**Atmospheric
Chemistry
and Physics**

Global NO$_x$ emission estimates derived from an assimilation of OMI tropospheric NO$_2$ columns

K. Miyazaki[1,2]**, H. J. Eskes**[1]**, and K. Sudo**[2,3]

[1]Royal Netherlands Meteorological Institute (KNMI), Wilhelminalaan 10, 3732 GK, De Bilt, The Netherlands
[2]Japan Agency for Marine-Earth Science and Technology, Yokohama 236-0001, Japan
[3]Graduate School of Environmental Studies, Nagoya University, Nagoya, Japan

Correspondence to: K. Miyazaki (miyazaki@knmi.nl)

Abstract. A data assimilation system has been developed to estimate global nitrogen oxides (NO$_x$) emissions using OMI tropospheric NO$_2$ columns (DOMINO product) and a global chemical transport model (CTM), the Chemical Atmospheric GCM for Study of Atmospheric Environment and Radiative Forcing (CHASER). The data assimilation system, based on an ensemble Kalman filter approach, was applied to optimize daily NO$_x$ emissions with a horizontal resolution of 2.8° during the years 2005 and 2006. The background error covariance estimated from the ensemble CTM forecasts explicitly represents non-direct relationships between the emissions and tropospheric columns caused by atmospheric transport and chemical processes. In comparison to the a priori emissions based on bottom-up inventories, the optimized emissions were higher over eastern China, the eastern United States, southern Africa, and central-western Europe, suggesting that the anthropogenic emissions are mostly underestimated in the inventories. In addition, the seasonality of the estimated emissions differed from that of the a priori emission over several biomass burning regions, with a large increase over Southeast Asia in April and over South America in October. The data assimilation results were validated against independent data: SCIAMACHY tropospheric NO$_2$ columns and vertical NO$_2$ profiles obtained from aircraft and lidar measurements. The emission correction greatly improved the agreement between the simulated and observed NO$_2$ fields; this implies that the data assimilation system efficiently derives NO$_x$ emissions from concentration observations. We also demonstrated that biases in the satellite retrieval and model settings used in the data assimilation largely affect the magnitude of estimated emissions. These dependences should be carefully considered for better understanding NO$_x$ sources from top-down approaches.

1 Introduction

Nitrogen oxides (NO$_x$) are important atmospheric species that affect atmospheric chemistry, air quality, and climate (IPCC, 2007). NO$_x$ dominantly controls the tropospheric ozone (O$_3$) budget, the abundance of the hydroxyl radical (OH), and the formation of nitrate aerosol. The reactions between NO$_x$ and hydrocarbons are major sources of O$_3$ in the troposphere. Tropospheric O$_3$ acts as a greenhouse gas and influences the lifetime of other greenhouse gasses. NO$_2$ also produces nitric acid (HNO$_3$) by reacting with OH, forming nitrate aerosols and acid particles. NO$_x$ has both anthropogenic and natural sources. Anthropogenic sources of NO$_x$ include fossil fuel and biofuel combustion, mainly emitted from power plants, transport (automobiles, ships, and aircrafts), and industry. Natural sources of NO$_x$ include soil, biomass burning, and lightning emissions. Dominant sinks of NO$_x$ in the troposphere are gas-phase formation of HNO$_3$ through reaction of NO$_2$ with OH especially during daytime and aerosol uptake of NO$_2$, NO$_3$, and N$_2$O$_5$. The lifetime of NO$_x$ is of the order of hours to days in the troposphere depending on various factors, including OH concentrations and photolysis rate (e.g. Lamsal et al., 2010). The short lifetime and the inhomogeneous source distribution of NO$_x$ result in obvious spatiotemporal variations in the NO$_2$ concentration in the troposphere.

Bottom-up NO$_x$ emission inventories from different sources and regions have large uncertainties. The extent of emission-related activities and emission factors used in the inventories are sources of error. Emission inventory information is often only available on a coarse resolution, such as country totals. In addition, simple multiplication factors are sometimes supplied with the emissions to describe the diurnal, weekly and seasonal dependence in an average way. Moreover, many emission sources have a large diurnal, weekly, or seasonal variability that is often poorly represented in the inventories. Examples are the traffic rush hour, wintertime heating of buildings (e.g. Streets et al., 2003), biomass burning events and their mid-day maxima, and the seasonality and pulses of soil emissions triggered by rainfall (e.g. Velders et al., 2001; Wang et al., 2007).

Observations of NO$_2$ concentrations provide important information on NO$_x$ emissions. Satellite retrievals provide better spatial coverage than in situ measurements, which can provide constraints on estimates of surface emissions. NO$_2$ can be measured as a column integral from solar backscatter instruments from space, since it absorbs light in the visible portion of the electromagnetic spectrum. Because the satellite measures an area-averaged amount of NO$_2$, satellite observations are more representative for the global model grid scale emissions than surface in situ local observations which depend strongly on (finer scale) local sources and local removal processes. Tropospheric NO$_2$ columns retrieved from satellite measurements, e.g. by Global Ozone Monitoring Experiment (GOME), GOME-II, Scanning Imaging Absorption Spectrometer for Atmospheric Cartography (SCIAMACHY), and Ozone Monitoring Instrument (OMI), have contributed to map spatiotemporal variations in NO$_x$ sources (e.g. Martin et al., 2003; Richter, 2004; van der A et al., 2006; Boersma et al., 2008b; Stavrakou et al., 2008; Kurokawa et al., 2009; Zhao and Wang, 2009; Lin et al., 2010). For instance, analyses of satellite data have identified rapid increases in NO$_x$ emissions over developing areas (e.g. Richter, 2004; van der A et al., 2006, 2008).

Top-down approaches adjust the emissions to reduce the discrepancy between the model and observation, while taking the errors in both model and retrievals into account. Martin et al. (2003) scaled bottom-up emissions directly based on the ratio of the local retrieved and model simulated columns. This approach has been widely applied to satellite retrievals owing to its simple implementation (e.g. Boersma et al., 2008b; Zhao and Wang, 2009; Lamsal et al., 2010). However, changes in emissions are not necessarily proportional to the local column changes because of atmospheric processes. For example, the NO$_2$/NO$_x$ ratio can vary owing to transport and chemical processes. To take these processes into account, recent studies have employed advanced data assimilation techniques including inverse modelling and four-dimensional variational assimilation (4D-VAR) (Müller and Stavrakou, 2005; Kurokawa et al., 2009; Chai et al., 2009). An ensemble Kalman filter (EnKF) is also an advanced data

assimilation technique (Evensen, 1994; Hunt et al., 2007) in which the forecast error covariance is advanced by the model itself (i.e. flow-dependent forecast error covariance). These advanced approaches allow us to fully take advantage of the chemical transport model (CTM). To the best of the authors' knowledge, no published research has yet been conducted to estimate global NO$_x$ emissions using EnKF to date.

In this study, we apply an EnKF data assimilation system to estimate daily global NO$_x$ emissions using OMI satellite retrievals and the Chemical Atmospheric GCM for Study of Atmospheric Environment and Radiative Forcing (CHASER) CTM (Sudo et al., 2002b). Using the data assimilation, we investigate the global distribution and the seasonal variation of surface NO$_x$ emissions. Even with such an advanced assimilation approach, however, the quality of both the model and the satellite retrieval will affect the accuracy of emission estimates (e.g. van Noije et al., 2006; Lamsal et al., 2010). Therefore, we will discuss the impact of model settings and biases in the satellite retrievals on the estimated emissions. The methodology is described in Sect. 2. The performance of the CTM is validated against satellite retrievals and presented in Sect. 3. An optimal data assimilation setting for NO$_x$ emission estimations is discussed in Sect. 4. Data assimilation and validation results against independent observations are presented in Sect. 5. The sensitivity of emission estimates to model settings and satellite retrieval are investigated in Sect. 6. Concluding remarks and discussions are provided in Sect. 7.

2   Methodology

Daily OMI tropospheric NO$_2$ column observations are used to constrain NO$_x$ emissions. The model simulation and assimilation results are validated using independent data, tropospheric NO$_2$ columns from SCIAMACHY measurements and vertical profiles obtained during the INTEX-B and the DANDELIONS campaigns. In this section, we introduce the model, the satellite data used in the assimilation, and the validation data sets.

2.1   Satellite and aircraft data

2.1.1   OMI data

The Dutch-Finnish OMI instrument, launched aboard the Aura satellite in July 2004, is a nadir viewing imaging spectrograph (Levelt et al., 2006). Aura traces a sun-synchronous, polar orbit with a period of 100 min. The local equator crossing time of Aura is about 13:40. OMI provides measurements of both direct and atmosphere-backscattered sunlight in the ultraviolet-visible range from 270 to 500 nm that is used to retrieve tropospheric NO$_2$ columns. OMI pixels are 13 km × 24 km at nadir, increasing in size to 24 km × 135 km for the largest viewing angles. OMI retrievals with their daily global coverage are effective to constrain global NO$_x$

emissions on a daily basis, different from GOME and SCIA-MACHY retrievals with poorer spatial and temporal resolutions and less global coverage.

The Dutch OMI tropospheric NO$_2$ (DOMINO) data product (Boersma et al., 2007) is used in this study. The DOMINO product is provided by the Tropospheric Emission Monitoring Internet Service (TEMIS) data portal (www.temis.nl). Since the sensitivity of nadir measurements varies with height, a priori vertical profile and averaging kernel (AK) information are important for the use of the observations in data assimilation (Eskes and Boersma, 2003). Detailed retrieval information is provided in DOMINO product, which allows proper use of observational information in data assimilation (cf. Sect. 2.3.1).

In the retrieval, the tropospheric air mass factors (AMFs) are computed at the time and location of the OMI overpass. The AMF measures the ratio of the slant column abundance to the vertical column abundance calculated from measured radiances with a radiative transport model. The AMF is determined by many factors; e.g. solar and viewing zenith angles, cloud fraction and cloud pressure derived using O$_2$-O$_2$ absorption, surface reflectivity, the a priori NO$_2$ profile simulated by a CTM, and the vertically resolved sensitivity to NO$_2$ of the solar radiation backscatter to space. Details of the retrieval and error estimates are described in Boersma et al. (2004). The retrieved tropospheric NO$_2$ column error is derived from errors in total slant column, its stratospheric portion, and the tropospheric AMF (Boersma et al., 2004, 2007). The error is dominated by the AMF calculation over polluted areas, whereas it is dominated by spectral fitting and stratosphere-troposphere separation over remote areas (Boersma et al., 2007). Only observations with a radiance reflectance of less than 50 % from clouds (i.e. cloud fraction less than about 20 %) are used in this study.

DOMINO v.1.03 data (hereafter DOMINO v1) released in 2008 generally shows good agreement with independent data, but appears to have a bias between 0 and 40 % (Boersma et al., 2011). Errors in the AMF may lead to high values for the AK and errors in the retrieval (Boersma et al., 2004, 2007; Lamsal et al., 2010). Boersma et al. (2011) describes improvements in the OMI retrieval, from DOMINO v1 to DOMINO v2.01 (hereafter DOMINO v2). The improvements include the description of the radiative transfer for the lowest atmospheric layers, assumptions made on surface albedo, terrain height, clouds, and sampling in a priori NO$_2$ profile. Tropospheric NO$_2$ columns retrieved from DOMINO v2 are about 20 % (10 %) lower in winter (in summer) compared to those from DOMINO v1 over polluted regions. We mainly use DOMINO v2 data to constrain NO$_x$ emissions.

2.1.2 SCIAMACHY data

SCIAMACHY was launched in March 2002 on board EN-VISAT (Bovensmann et al., 1999). We use tropospheric NO$_2$

data from the KNMI retrieval algorithm and the observation data were obtained from the TEMIS data server (Boersma et al., 2004). The ground pixel of the nadir mode is generally 60 by 30 km^2, with a global coverage approximately once every six days. The local overpass time is 10:00. The approach to calculate the AMF is almost the same as that for DOMINO v1 data, while DOMINO v2 is a major update with several changes to the AMF computation. Errors in the slant column fitting, the stratospheric corrections, and in the AMFs lead to an overall error in the SCIAMACHY retrieval, as described in Boersma et al. (2004). The retrieval was validated against in situ and aircraft measurements, and was compared with regional air quality models (e.g. Schaub et al., 2007; Blond et al., 2007).

As discussed by Boersma et al. (2007) and Lin et al. (2010), systematic errors in OMI (DOMINO v1) and SCIA-MACHY retrievals are expected to correlate well with each other, since these retrievals are derived with a very similar algorithm. Differences between OMI and SCIAMACHY retrievals thus mainly reflect temporal (diurnal) variations of chemical processes and emissions. As an exception, the improvements in DOMINO v2 may create systematic differences between the DOMINO v2 and the SCIAMACHY retrievals. The size of viewing pixels is different between the retrievals. In comparison with model and assimilation results, both retrievals are gridded to the same resolution ($2.5 \times 2.5°$), using weighting factors for the surface overlap between satellite pixel and grid cell. As a result, the viewing pixel size difference will not affect the comparison results too much.

2.1.3 INTEX-B aircraft data

The in situ vertical profile data were obtained using the UC Berkeley Laser-Induced Fluorescence (TD-LIF) instrument on DC-8 during the Intercontinental Chemical Transport Experiment Phase B (INTEX-B) campaign over the Gulf of Mexico (Singh et al., 2009). Thornton et al. (2003) and Bucsela et al. (2008) provide a detailed description and discuss the performance of the measurement. In the comparison between model and assimilation results, the data were binned on a pressure grid, with an interval of 30 hPa, whereas the model output was interpolated to the time and space of each sample. The standard deviation of variability within a grid cell is considered to represent the uncertainty. Data collected over highly polluted areas (over Mexico City and Houston) have been removed from the comparison, since it can cause a serious representativeness error in the comparison (i.e. the model resolution is too coarse). The comparisons were made for morning (08:00 a.m.–10:00 a.m.) and afternoon (02:00 p.m.–04:00 p.m.) conditions in March 2006.

2.1.4 DANDELIONS lidar data

The Netherlands National Institute for Public Health and the Environment (RIVM) NO$_2$ lidar uses the Differential Absorption Lidar (DIAL) technique to observe vertical NO$_2$ profiles. Volten et al. (2009) provides a detailed description of the measurement during the Dutch Aerosol and Nitrogen Dioxide Experiments for Validation of OMI and SCIAMACHY (DANDELIONS) campaign. In comparison with the lidar data, the model output was interpolated to each sampling level of the lidar at Cabauw. The results were binned on a height grid, with an interval of 100 m. Lidar profiles have a spatial representation of 2 km in the viewing direction and approximately 12 km in the direction of the wind. The model resolution is much coarser and thus the observation has a large representativeness error. The model grid points used for the interpolation around Cabauw are located at Belgium, northern-eastern Netherlands, western Germany, and on the North Sea. Boundary layer conditions are very different among the grid points especially between land and ocean. To avoid a possible large representativeness error in particular under the different boundary layer condition, the profiles obtained only before 12:00 p.m. were used for the comparison.

2.2 A global chemical transport model CHASER

A global CTM for the troposphere, CHASER, developed by Sudo et al. (2002b), is used as a forecast model in the data assimilation system. CHASER includes detailed chemical and transport processes in the troposphere, including 88 chemical and 25 photolytic reactions with 47 chemical species. CHASER is coupled to the atmospheric general circulation model, Center for Climate System Research/National Institute for Environmental Studies/Frontier Research Center for Global Change (CCSR/NIES/FRCGC) atmospheric general circulation model (AGCM) ver. 5.7b, on a horizontal resolution of T42 (2.8°) and 32 vertical levels from the surface to 4 hPa. Meteorological fields are provided by the AGCM at every time step of CHASER (i.e. every 20 min), in which the AGCM fields are nudged toward National Centers for Environmental Prediction/Department of Energy Atmospheric Model Intercomparison Project II (GPS-NCEP/DOE AMIP-II) reanalyses (Kanamitsu et al., 2002) at every time step of the AGCM to reproduce past meteorological conditions. The transport processes include sub grid-scale (parameterized) convective transport and vertical diffusion in addition to grid-scale advection. A more detailed description of the CHASER model is presented by Sudo et al. (2002b), Sudo and Akimoto (2007), and Nagashima et al. (2010). The extensive evaluation of the overall CHASER model performance was performed by Sudo et al. (2002a). The relative performance of the CHASER NO$_2$ simulation in comparison to other CTMs is evaluated by van Noije et al. (2006).

The anthropogenic emissions of NO$_x$ are based on an inventory of national emissions obtained from the Emission Database for Global Atmospheric Research (EDGAR) version 3.2 for the year 1995 and 2000 (Olivier et al., 2005), which are reported as yearly means. Emissions from biomass burning are determined on a monthly basis according to the satellite-derived carbon emission estimates from the Global Fire Emissions Data base (GFED) version 2.1 (Randerson et al., 2007). NO$_x$ emissions from soils are based on Global Emissions Inventory Activity (GEIA) (Graedel et al., 1993), which are reported as monthly means. NO$_x$ emissions over Asia were obtained from Regional Emission inventory in Asia (REAS) version 1.1 (Ohara et al., 2007) for the year 1995 and 2000. For all emission categories, the emission values for the simulation years 2005–2006 are obtained by extrapolating the emission inventories from the years 1995 and 2000. Total amounts of these surface NO$_x$ emissions for January, April, July, and October in 2005 are 42.9, 37.6, 46.3, and 39.2 TgN yr^{-1}, respectively. The monthly/yearly emission data were linearly interpolated at each time step of the CHASER and used in the simulation. The total lightning NO$_x$ production is globally scaled to 7.5 TgN yr^{-1}, and its distribution is calculated at each time step of CHASER using the convection scheme in the AGCM and the parameterization of Price and Rind (1992). The total aircraft NO$_x$ emission is 0.55 TgN yr^{-1}, which is obtained from the EDGAR inventory.

We apply a diurnal variability scheme to the emissions depending on the dominant category for each area: anthropogenic, biogenic, and soil emissions. Note that a diurnal scaling of each emission category separately is a more logical approach. However, this approach cannot be applied in this study since only the total emission is processed in the model simulation. van der A et al. (2008) determined the dominant source categories for each area based on the analysis of the seasonality of observed tropospheric NO$_2$ column. Following the result of van der A et al. (2008) and the setting of Boersma et al. (2008b), we apply anthropogenic-type diurnal variations (with maxima in morning and in evening with a factor of about 1.4) in Europe, eastern China, Japan, and North America; biomass burning-type variations (with a rapid increase in morning and maximal emissions in the midday with a maximum factor of about 3) in central Africa and South America; and soil-type diurnal variations (with maximal emissions in afternoon with a factor of about 1.2) in the grasslands or sparsely vegetated areas of Australia, Sahara, and western China. The soil NO$_x$ emission dependence on temperature and moisture (Yienger and Levy, 1999) is not explicitly considered. The total amount of emissions does not change by applying the diurnal variability scheme.

2.3 Data assimilation

Data assimilation is a technique to combine observational information with a model. We employ an ensemble Kalman

filter approach to estimate NO$_x$ emissions from NO$_2$ data. The assimilation runs were performed for six individual months (starting from 1st to 30th of each month), January, April, July, and October in 2005, and March and September in 2006. The initial conditions for meteorological and chemical fields were obtained from long-term (about a year) simulation of the CHASER for each month. The results for 2005 are used to investigate the seasonal variability of the emission, while those for 2006 are used to validate the assimilation results against in situ observations.

2.3.1 Ensemble Kalman filter

The data assimilation technique employed is a local ensemble transform Kalman filter (LETKF). There are two types in EnKF approaches, the perturbed observation (PO) method and the ensemble square root filter (SRF) method (e.g. Whitaker and Hamill, 2002). SRF methods generate an analysis ensemble mean and covariance that satisfy the Kalman filter equations for linear models (e.g. Ott et al., 2004), whereas PO methods introduce an additional source of sampling errors. The LETKF is related to the SRF method (e.g. Whitaker and Hamill, 2002), and it has conceptual and computational advantages over the original EnKF (e.g. Ott et al., 2004; Hunt et al., 2007; Kalnay, 2010). One of the advantages is that the LETKF performs the analysis locally in space and time, and reduces sampling errors caused by a limited ensemble size. In addition, the analyses at different grid points are performed independently, which reduces the computational cost because most calculations are performed in parallel in the LETKF (e.g. Miyoshi and Yamane, 2007).

Here we briefly introduce the LETKF technique following Hunt et al. (2007) and Kalnay (2010). The LETKF updates the analysis and transforms a background ensemble ($\mathbf{x}_i^b; i = 1, \ldots, k$) into an analysis ensemble ($\mathbf{x}_i^a; i = 1, \ldots, k$), where $\mathbf{x}$ represents the model variable; b the background state; a the analysis state; and k the ensemble size. In the forecast step, a background ensemble, $\mathbf{x}_i^b$, is globally obtained from the evolution of each ensemble member using the forecast model. The background ensemble mean, $\overline{\mathbf{x}^b}$, and its perturbations (spread), $\mathbf{X}^b$, are estimated from the ensemble forecast,

$$\overline{\mathbf{x}^b} = \frac{1}{k} \sum_{i=1}^{k} \mathbf{x}_i^b \; ; \;\; \mathbf{X}_i^b = \mathbf{x}_i^b - \overline{\mathbf{x}^b}. \tag{1}$$

These are $N \times k$ matrices, where N indicates the system dimension and k indicates the ensemble size. The background error covariance follows from the assumption that background ensemble perturbations $\mathbf{X}^b$ sample the forecast errors,

$$\mathbf{P}^b = \mathbf{X}^b (\mathbf{X}^b)^T. \tag{2}$$

In the analysis step, an ensemble of background vectors, $\mathbf{y}_i^b$, and an ensemble of background perturbations in the observation space, $\mathbf{Y}^b$, are obtained as follows:

$$\mathbf{y}_i^b = H\left(\mathbf{x}_i^b\right); \mathbf{Y}^b = \mathbf{y}_i^b - \overline{\mathbf{y}^b}, \tag{3}$$

where H is the non-linear observational operator that converts an N-dimensional state vector to a p- (number of observation) dimensional observational vector. To compute the analysis for each grid point independently, the local analysis error covariance is estimated in the ensemble space:

$$\tilde{\mathbf{P}}^a = \left[\frac{(k-1)\mathbf{I}}{1+\Delta} + \left(\mathbf{Y}^b\right)^T \mathbf{R}^{-1} \mathbf{Y}^b \right]^{-1}, \tag{4}$$

where $\mathbf{R}$ denotes the $p \times p$ observation error covariance. To prevent an underestimation of background error covariance and resultant filter divergence (e.g. Houtekamer and Mitchell, 1998) caused by model errors and sampling errors, the covariance inflation technique (with a covariance inflation parameter $\Delta = 0.05$ in our setting, see also Sect. 4.2) is applied to inflate the forecast error covariance at each analysis step.

Using $\tilde{\mathbf{P}}^a$, the transformation matrix, $\mathbf{T}$, is given by,

$$\mathbf{T} = \left[(k-1)\tilde{\mathbf{P}}^a \right]^{1/2} \tag{5}$$

$\mathbf{T}$ is a $k \times k$ matrix which analyzes the variables for each grid point (Hunt et al., 2007). The dimension k is generally smaller than N, and calculations of large vectors or matrices with N dimension are not necessary to obtain the $\mathbf{T}$ matrix in the LETKF, which is different from the case for the original EnKF. Then, we can update the ensemble mean by

$$\overline{\mathbf{x}}^a = \overline{\mathbf{x}}^b + \mathbf{X}^b \tilde{\mathbf{P}}^a \left(\mathbf{Y}^b\right)^T \mathbf{R}^{-1} \left(\mathbf{y}^o - \overline{\mathbf{y}^b}\right), \tag{6}$$

where $\mathbf{y}^o$ represents the observation vector. The new analysis ensemble perturbation matrix in the model space $\mathbf{X}^a$ is simultaneously obtained by transforming the background ensemble $\mathbf{X}^b$ with a transform matrix $\mathbf{T}$ at every grid point ($\mathbf{X}^a = \mathbf{X}^b \mathbf{T}$), while the new analysis ensemble in the model space, $\mathbf{x}_i^a$, is obtained from the combination of the background mean and ensemble perturbations ($\mathbf{x}_i^a = \overline{\mathbf{x}}^a + \mathbf{X}_i^a$).

The EnKF approaches always have a spurious long distance correlation problem because of imperfect sampling of the probability distribution due to limited ensembles (e.g. Houtekamer and Mitchell, 2001). To improve the performance of the data assimilation with reducing the ensemble size, the LETKF employs a covariance localization technique. We assumed that observations located far from the analysis point have larger errors and those observations have less impact on the analysis (e.g. Miyoshi and Yamane, 2007). As a result, the analysis is solved at every grid point by choosing nearby observations (depending on the localization length, see Sect. 4.2).

The tropospheric AK provided in the OMI retrieval product is used in the assimilation. The use of the average kernel in the observation operator removes the contribution of

the retrieval error due to the a priori profile error (Eskes and Boersma, 2003);

$$\mathbf{y}_i^b = H\left(\mathbf{x}_i^b\right) = \sum_{l=1}^{L} a_l S_l\left(\mathbf{x}_i^b\right), \tag{7}$$

where a_l is the components of the AK at the l-th vertical level. The spatial interpolation operator S_l contains a horizontal interpolation followed by a mass-conserving vertical interpolation to the OMI retrieval level l and a conversion to NO$_2$ sub-columns. Simulated NO$_2$ fields in this way are converted into tropospheric NO$_2$ columns using the AK, the surface pressure obtained from the AGCM simulation, and the tropopause level L used in the OMI retrieval product.

In summary, the LETKF analyzes variables (i.e. NO$_x$ emissions) for every grid point by choosing observations (i.e. OMI retrievals) that determine the observational space. Then, the analysis is solved independently at every grid point located at the local volume center using the observational information and background error covariance estimated from the ensemble forecast. The new global analysis ensemble of the variables (i.e. NO$_x$ emissions) is then obtained by combining the local analysis. The estimated emissions are used in the next step ensemble model simulations (after the forecast process) and updated at every analysis step. The forecast and analysis processes for NO$_x$ emissions are further described in Sect. 2.3.2.

2.3.2 NO$_x$ emission estimation

A top-down approach with a bottom-up emission inventory (as a priori) was used to obtain posterior estimates of surface NO$_x$ emissions. To accomplish this, we applied the state augmentation method (e.g. Aksoy et al., 2006). In this method, the model parameter (i.e. NO$_x$ emission, $\mathbf{e}$) is estimated by including it as part of the state vector together with the model forecast variable (i.e. NO$_2$ concentration, $\mathbf{c}$) using the ensemble model simulations and observations. The background ensemble and its perturbations defined in Eq. (1) thus become,

$$\mathbf{x}_i^b = \begin{bmatrix} \mathbf{c}_i^b \\ \mathbf{e}_i^b \end{bmatrix}; \quad \mathbf{X}_i^b = \begin{bmatrix} \mathbf{c}_i^b - \overline{\mathbf{c}_i^b} \\ \mathbf{e}_i^b - \overline{\mathbf{e}_i^b} \end{bmatrix}. \tag{8}$$

This approach allows indirect relationships between NO$_2$ concentrations and NO$_x$ emissions caused by complex chemical and transport processes (e.g. changes in the NO$_2$/NO$_x$ ratio) to be considered through the use of the background error covariance produced by ensemble CTM forecasts. This advanced approach differs from methods based on the modeled local ratio between concentrations and emissions (e.g. Martin et al., 2003). In our approach, the background error covariance, estimated from the ensemble CTM simulations, varies with time and space depending on atmospheric conditions. Accordingly, the local analysis increment, which is the a posteriori emission minus the a priori emission, is not

solely determined by the difference in the observed and simulated concentrations.

The forecast process also plays important roles in the data assimilation. It propagates observation information, inflates the analysis spread, and determines the quality of the first guess. A linearized forecast model ($\mathbf{M}$) provides a first guess of the state vector for data assimilation based on the background error covariance from the previous analysis time t_n to the new analysis time t_{n+1},

$$\mathbf{P}^b\left(t_{n+1}\right) = \mathbf{M}\mathbf{P}^a\left(t_n\right)\mathbf{M}^T + \mathbf{Q}. \tag{9}$$

In this study, because of the lack of any applicable model, a persistent forecast model ($\mathbf{M} = \mathbf{I}$) is used for the NO$_x$ emissions. In our setting, without any treatment that prevents the parameter covariance magnitude reduction (e.g. by the forecast model error covariance term $\mathbf{Q}$), the analysis can no longer be influenced by the observations, because of an overestimation of the confidence in the model. To prevent covariance underestimation, the analyzed standard deviation (i.e. background error) is artificially inflated back to a minimum predefined value at each analysis step. This minimum value used in this study is chosen as 30 % of the initial standard deviation (see also below). The analysis spread can be very small in some cases owing to effective corrections by the data assimilation. Because of the inflation in our daily analysis, the emission analysis can capture short-term variations of NO$_x$ emissions. This is different from some previous studies that estimated emissions based on monthly mean data (e.g. Martin et al., 2003; Wang et al., 2007; Chai et al., 2009; Kurokawa et al., 2009). A daily analysis improves upon the monthly-mean inversion by accounting for the variability in the chemical feedbacks of NO$_x$ emissions and by reducing the dependence of the a priori emissions (Zhao and Wang, 2009). Small random noises were also added to the analysis spread as the random forecast model error after the covariance inflation at each analysis step, with a magnitude of 4 % of the initial spread. The minimum predefined ensemble spread of 30 % and the random noise magnitude of 4 % used in data assimilation were obtained from sensitivity experiments by changing the predefined magnitude to 15, 30, 45, and 60 %, and the noise magnitude to 0, 4, 8, and 12 %, respectively. Quantitative criteria for the selection of these values are the daily Observation-minus-Forecast (OmF) check and the chi-square (χ^2) test (see Sect. 4.2 for details). The optimal values of 30 % and 4 % were obtained by minimizing the global mean and root mean square of the OmF and by requiring that χ^2 value approaches 1.

Uncertainty information on the a priori emission is required to create the initial emission error covariance. We expect large uncertainty in the a priori emission, as a result of the neglected seasonality in the anthropogenic emissions and large discrepancy between different anthropogenic (e.g. EDGAR vs. REAS) and biomass burning emission inventories (e.g. EDGAR vs. GEIA). The initial error is set to

40 % of the a priori emission. Note that the emission analysis is generally no longer sensitive to the initial error after some (e.g. several weeks) assimilation cycles. Only the combined total emission is optimized in the analysis. This is to reduce the degree of freedom in the analysis and to avoid the difficulty associated with estimating background errors for each category source separately. The uncertainty in the a posteriori emission is reduced if the analysis converges to a true state, which is represented by the analysis spread in the EnKF data assimilation. For instance, in January, the mean analysis spread becomes about 30–40 % of the initial spread after some assimilation cycles over northern Europe, the United States North, America, eastern China, India, and northern Africa, demonstrating significant reductions in the emission uncertainty through the data assimilation over these areas. However, since the analysis spread is artificially inflated to the predefined constant value during the analysis step in our system, this information is not used to measure the a posteriori uncertainty. Instead, the standard deviations of the estimated daily emissions during the analysis period are used as the uncertainty information. Detailed analyses on the analysis spread information will be performed using more advanced inflation techniques in future studies (see also discussions in Sect. 4.2).

The surface emission factor is analyzed and updated using observations at an analysis interval of every 100 min (i.e. every orbit cycle of OMI observations). This setting is useful to reduce the time discrepancy between the observation and the model in the data assimilation. Tropospheric NO$_2$ shows a distinct diurnal variation, and any time discrepancy will result in serious model error.

2.3.3 Super-observation approach

The spatial resolution of the OMI data ($=13$ km $\times 24$ km) is much finer than that of the CHASER model grid ($=2.8°$). Thus, there are large representativeness errors in the model because of unresolved small-scale variations. To fill the spatial scale gaps and to produce more representative data, a super-observation approach has been developed. The spatial resolution of the super-observation was set to be $2.5°$, almost equivalent to the CHASER model resolution. Note that the spatial distribution of the super-observation is constant, whereas the CHASER uses a Gaussian (variable) grid. A super-observation is generated by averaging all data located within a super-observation grid cell;

$$\overline{y} = \left(\sum_{l=1}^{m} w_l y_l \right) \bigg/ \left(\sum_{l=1}^{m} w_l \right), \tag{10}$$

where $\overline{y}$ is the super-observation concentration; y_l is the concentration of individual data; w_l is the weighting factor; m is the number of observations within a super-observation grid. The weighting factor for individual data, w_l, is estimated as the ratio of the coverage area by individual data pixels and the total coverage area (sum of the coverage area by all data used

for generating a super observation) for a super-observation grid; i.e. data with high coverage are assumed to be more reliable (i.e. larger w_l). The same weighting factors are applied for averaging the AK.

The measurement error for the super-observation is computed as in Eskes et al. (2003),

$$\sigma_{\text{super, mean}} = \left(\left(\sum_{l=1}^{m} w_l \sigma_l \right) \bigg/ \left(\sum_{l=1}^{m} w_l \right) \right) \sqrt{\frac{1-c}{m} + c}, \tag{11}$$

in which the observation error (σ_l) is averaged over a grid with the weight (w_l), and the averaged error is multiplied by the error correlation (c) among data. The error correlation determines the quality of the super-observation, as illustrated in Fig. 1a. We apply 15 % error correlation, although there is no evidence for this value. Errors in for instance the cloud, albedo and aerosol treatment in the NO$_2$ retrieval are typically correlated in space, but a quantitative number for this correlation is difficult to estimate. The super-observation measurement error also decreases as the number of observations used for the super-observation increases. A typical number of OMI observations used for a super-observation is about 120–250, resulting in about 60 % reduction of the mean measurement error.
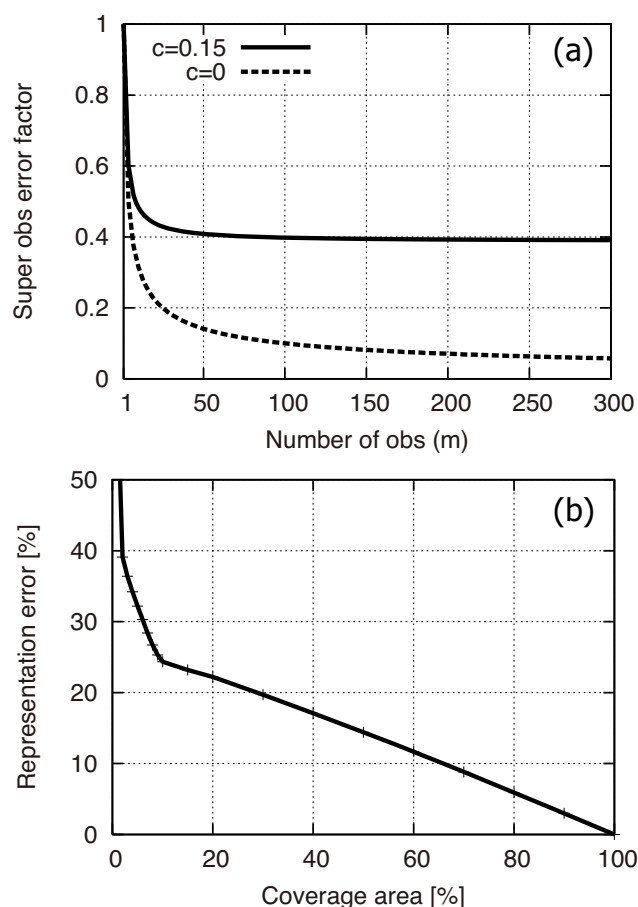
The representativeness error is also considered if the super-observation grid is not fully covered by OMI pixels. A representativeness error as a function of the OMI coverage was estimated based on grid cells which were well-covered by OMI pixels (i.e. more than 90 % coverage, excluding remote areas where the mean concentration is less than 0.5×10^{15} molec. cm^{-2}). For these well-covered cells, we artificially decreased the coverage by randomly reducing the number of observations used for constructing a super-observation. Then, a representativeness error factor (f_{rep}) is estimated based on the relationships between the coverage area (α, $0 < \alpha \leq 1$) and the super-observation concentration as follow;

$$f_{\text{rep}}(\alpha) = \left| \left(\frac{1}{m} \sum_{l=1}^{m} y_l - \frac{1}{\alpha \times m} \sum_{l=1}^{\alpha \times m} y_l \right) \bigg/ \left(\frac{1}{m} \sum_{l=1}^{m} y_l \right) \right|. \tag{12}$$

For coarse grid cells completely covered by OMI observation footprints ($\alpha = 1$), this representativeness error is zero. For cells covered by just one OMI pixel the representativity error approaches the variability of individual measurements around the grid cell mean. The mean representativeness error factor averaged over the globe and over a month almost linearly increases as the coverage decreases, with a steeper increase for coverage area less than 10 % (Fig. 1b). The mean averaged function is applied to estimate the representativeness error of each super-observation according to its coverage areas (α):

$$\sigma_{\text{super, rep}} = f_{\text{rep}}(\alpha) \times \overline{y} \tag{13}$$

where the area dependence of the representativeness error function was neglected. Finally, the total super-observation

Fig. 1. (a) The error reduction factor for the super-observation as a function of number of observations, m, for different sub-grid error correlations, $c = 0$ (dotted line) and 15 % (solid line). **(b)** The representativeness error multiplication factor f_{rep} as a function of the coverage of the grid cell by OMI observations. See Eqs. (11) and (12) and Sect. 2.3.3 for details.

error is computed as a combination of the measurement error and the representativeness error, $\sqrt{\sigma^2_{\text{super,mean}} + \sigma^2_{\text{super,rep}}}$.

3　Simulated and retrieved tropospheric NO$_2$ columns

Here we investigate the performance of the model and satellite retrievals. The AK has been applied to the CHASER profiles to compare with satellite retrievals precisely. The CHASER concentrations are interpolated to the retrieval pixels at the local overpass time of the satellite, and then both the retrieved and simulated concentrations are mapped onto a same horizontal resolution of $2.5 \times 2.5°$.

3.1　Global distribution

Figure 2 compares global distributions of annual-mean tropospheric NO$_2$ columns obtained from the OMI retrievals, the SCIAMACHY retrieval, and the CHASER simulation at the local overpass time of the retrievals (10:00 and 13:30, respectively). The retrievals and the model show very similar spatial distributions. Large-scale pollution with high concentrations is observed over eastern China, Europe, and the eastern United States. High concentrations are also found over the Highveld region of southern Africa, central Africa, Japan, South Korea, India, Southeast Asia, and other mega cities. Low concentrations, mostly smaller than the OMI noise level, are observed over the oceans and remote regions. Note that the annual-mean distribution in both the model and retrievals may be positively biased compared to the true annual-mean local time NO$_2$ concentration. This occurs especially over tropical regions, since the sampling under clear sky condition leads to relatively fewer observations during the wet seasons than during the dry seasons (van Noije et al., 2006).

The OMI retrievals agree well with the SCIAMACHY retrieval, with a global spatial correlation of 0.90–0.93, a global mean root-mean-square error (RMSE) of about 0.35–0.66×10^{15} molec. cm^{-2}, and the global mean bias (OMI minus SCIAMACHY) of -0.02–0.12×10^{15} molec. cm^{-2} for the monthly mean concentration. The OMI mean difference compared to the SCIAMACHY is mostly positive and is larger for DOMINO v1 than DOMINO v2, whereas the RMSE compared to the SCIAMACHY retrieval is higher for DOMINO v2 than DOMINO v1. Higher concentrations are observed in DOMINO v1 than in DOMINO v2 over northern Europe, the northern-eastern United States, and eastern China, with a mean difference of about 10–30 % (Fig. 2). Apart from the global mean, the SCIAMACHY retrieval shows higher NO$_2$ concentrations than the OMI retrievals over urban areas around megacities and lower concentrations over biomass burning regions (Boersma et al., 2008b), probably mainly as a result of the difference in observation time.

Although CHASER reproduces well the general features of the observed NO$_2$ patterns (with a global spatial correlation of 0.71–0.89 depending on season and retrieval, similar to that estimated using other global CTMs (van Noije et al., 2006; Huijnen et al., 2010), systematic differences exist between the model and retrievals (Table 1). The model is generally negatively biased relative to the OMI retrievals, but is positively biased relative to the SCIAMACHY retrieval (except in January) in the global mean. This may be partly due to the bias observed between the SCIAMACHY and OMI, dominated by the background concentrations smaller than the detection limit of OMI and the stratospheric contribution to the column. The model generally underestimates tropospheric NO$_2$ columns in industrial areas (Fig. 2); e.g. over eastern China, the eastern United States, southwestern Europe, and southern Africa, suggesting that

anthropogenic emissions in the emission inventories are underestimated. As an exception, the model largely overestimates NO$_2$ columns over northern Europe, particularly when compared to DOMINO v2. The model negative bias is also observed over biomass burning areas; e.g. over central Africa and South America. In contrast, significant positive model biases exist in remote areas especially when compared to the SCIAMACHY data. The RMSE is largest in January in all cases.

By applying the AK, the model generally shows better agreements with satellite retrievals, as commonly found using other CTMs (van Noije et al., 2006; Huijnen et al., 2010). The application of the AK increased the global spatial correlation by 0.02–0.13, decreased the global mean bias by 0.01–0.32 (up to about 90 %), with larger impacts on the comparison with the SCIAMACHY retrieval than that with the OMI retrievals. The larger impacts with the SCIAMACHY AK may be attributed to larger differences between the a priori used in the SCIAMACHY retrieval and the CHASER profiles. The impact was significant over Europe and eastern Asia and was different among seasons. For instance, the application of DOMINO v1 AK leads to a change of NO$_2$ column up to -1.1×10^{15} molec. cm^{-2} ($+1.5 \times 10^{15}$ molec. cm^{-2}) over Europe in January (July). The increase (decrease) implies a larger (smaller) decrease of NO$_2$ concentration with height in the a priori profile used in the retrieval than in the profile simulated by the CHASER. For the OMI comparisons, the impact of the AK was weaker in the case of the DOMINO v2 than the DOMINO v1 over polluted areas, suggesting that the CHASER profile is more similar to the a priori profile used in DOMINO v2 than that in DOMINO v1.

3.2 Seasonal variation

Figure 3 compares the seasonal variations of the regional mean tropospheric NO$_2$ columns for major polluted and biomass burning areas. The seasonal variations are very similar among the satellite retrievals, except for clear differences between DOMINO v1 and v2 over Europe, the eastern United States, and southern Africa during winter. In industrial regions, the tropospheric NO$_2$ column is higher in winter than in summer. Biomass burning occurs especially during the dry season, in the winter and early spring, leading to a maximum concentration in these seasons over the central Africa, Southeast Asia, and South America. The simulated regional mean tropospheric NO$_2$ columns are generally lower than the observed ones in most polluted regions throughout the year. The underestimation is more obvious in winter than in other seasons over eastern China, the eastern United States and southern Africa. A most obvious difference is seen over eastern China and southern Africa with a factor of up to 3. The timing of the seasonal variation is well represented, but the amplitude is largely underestimated by the model over these regions. Over central Africa, South

America, and Southeast Asia, biomass burning dominates the seasonal variations of NO$_2$ concentrations, where the maximum and minimum concentration occurs almost in the same months in the model and retrievals, but with a mean negative bias of about 20–40 % in the model.

3.3 Diurnal variation

To improve the simulation, we applied pre-defined functions for the diurnal variations of the surface NO$_x$ emissions. As described in Sect. 2.2, we applied different diurnal variation profiles for different sources: maxima in the morning and evening for anthropogenic sources; a rapid increase in the morning and maximal emissions at mid-day for biomass burning sources; and maximal emissions in the afternoon for soil sources. By applying the diurnal variability scheme, CHASER generally shows better agreement with the satellite retrievals, with a global mean RMSE reduction of about 10–15 (30–40) % compared to the OMI (SCIAMACHY) retrievals. Similar results were demonstrated with other CTMs (van Noije et al., 2006; Boersma et al., 2008b). The diurnal variability scheme generally decreases the NO$_2$ concentration in the morning, but increases it in the afternoon in the industry and biomass burning areas (Fig. 4). It improves the agreement with DOMINO v2 data over Europe (Fig. 4a), whereas the increased biomass burning emission during daytime caused the NO$_2$ columns over Central Africa to be too high compared to DOMINO v2 data (Fig. 4b). The diurnal variability for the biomass burning source is highly variable and uncertain. Since the diurnal variation of NO$_x$ emissions strongly influences the model-observation difference, the implementation of a realistic diurnal scheme is important to obtain reasonable emissions. The impact of the diurnal scheme on surface emission estimations will be further discussed in Sect. 6.

4 Optimizing the data assimilation system

4.1 Impact of super-observation

By using the super-observations instead of the normal observations, the data assimilation reveals a better agreement with the assimilated DOMINO v2 data. An increasing spatial correlation of 0.03–0.05 and a decreasing global mean RMSE of 30–40 % were observed in an experiment with the super-observations compared to normal observations. Improvements by the super-observation approach were commonly observed at both a resolution of the super-observations (i.e. 2.5°) and at finer scale (i.e. 1°). In the case with the normal observations, observation data contain large representativeness error and are noisy especially in polluted areas, which may prevent the analysis from efficiently and stably reducing the systematic errors of the model (i.e. analysis increments were sometime very noisy and large). The super-observation approach generally provides more representative
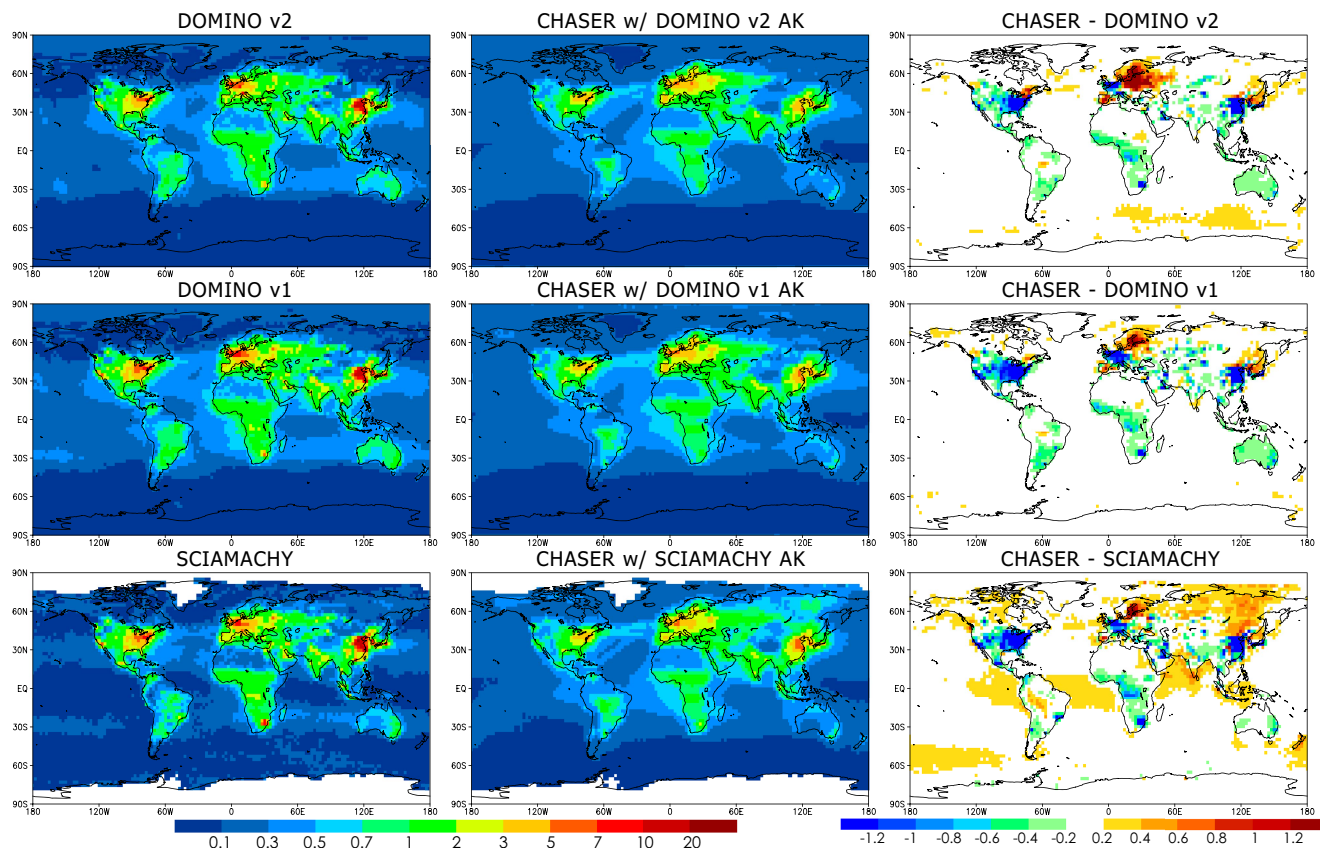
Fig. 2. Global distributions of annual mean tropospheric NO$_2$ columns (in 10^{15} molec. cm^{-2}) obtained from the satellite retrievals (left columns): DOMINO v2 (upper rows), DOMINO v1 (middle rows), and SCIAMACHY (lower rows), and from the CHASER simulation estimated using the AK of each retrieval to be compared with the simulation (middle columns) for 2005. The red (blue) colour indicates relatively high (low) values. The differences between the retrievals and the CHASER simulation (the simulation minus the retrievals) are shown in the right columns; the red (blue) colour indicates that the CHASER is larger (smaller) than the satellite retrievals.

Table 1. Comparisons of monthly and annual mean tropospheric NO$_2$ columns between the CHASER simulation (applying the AK of each retrieval) and the satellite retrievals: DOMINO v1, DOMINO v2, and SCIAMACHY, for 2005. The RMSE is the root-mean-square error. The bias represents the CHASER simulation minus the retrievals. The units for the RMSE and bias are 10^{15} molec. cm^{-2}.

		JAN	APR	JUL	OCT	ANN
	Corr	0.71	0.88	0.90	0.88	0.86
vs. DOMINO v2	RMSE	0.79	0.36	0.28	0.41	0.38
	Bias	−0.01	−0.02	−0.07	−0.08	−0.03
	Corr	0.77	0.88	0.89	0.89	0.89
vs. DOMINO v1	RMSE	0.92	0.44	0.31	0.48	0.44
	Bias	−0.11	−0.07	−0.07	−0.12	−0.06
	Corr	0.76	0.82	0.79	0.80	0.86
vs. SCIAMACHY	RMSE	1.03	0.57	0.51	0.53	0.53
	Bias	−0.06	0.06	0.04	0.00	0.01
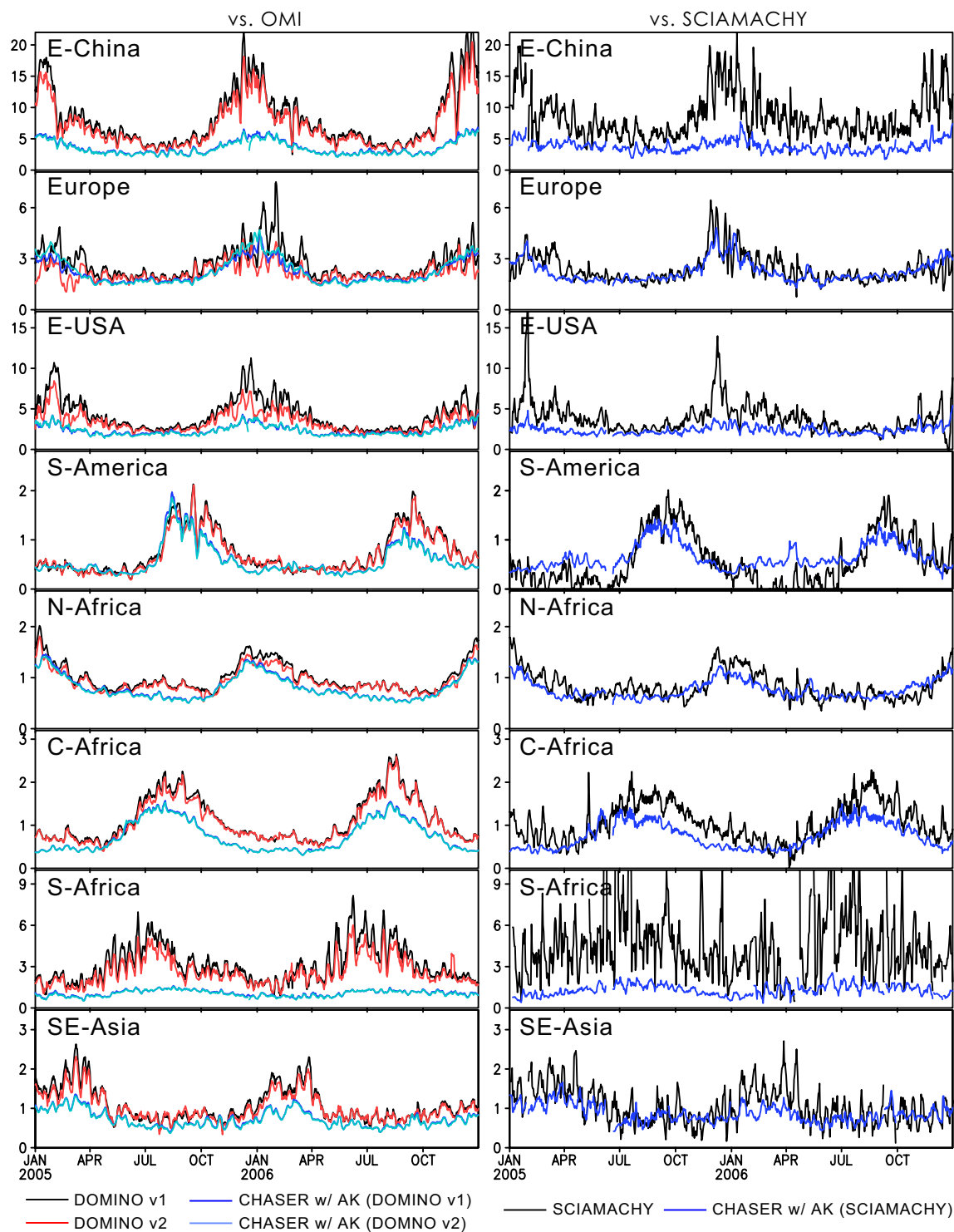
Fig. 3. Seasonal variations of the regional mean tropospheric NO$_2$ columns (in 10^{15} molec. cm^{-2}) for eastern China (110–123° E, 30–40° N, top panels), Europe (10° W–30° E, 35–60° N, second-top panels), the eastern United States (95–71° W, 32–43° N, third-top panels), South America (70–50° W, 20° S–Equator, fourth-top panels), northern Africa (20° W–40° E, Equator–20° N, fifth-top panels), central Africa (10–40° E, 20° S–Equator, sixth-top panels), southern Africa (26–31° E, 28–23° S, seventh-top panels), and Southeast Asia (96–105° E, 10–20° N, bottom panels) for 2005–2006. Tropospheric NO$_2$ columns obtained from DOMINO v2 (red lines in left panels), DOMINO v1 (black lines in left panels), the SCIAMACHY retrieval (black lines in right panels), and the CHASER simulation with the AK (blue and light blue lines) are plotted for local time 13:30 (left) and 10:00 (right). A 4-day running-mean was applied to the data.
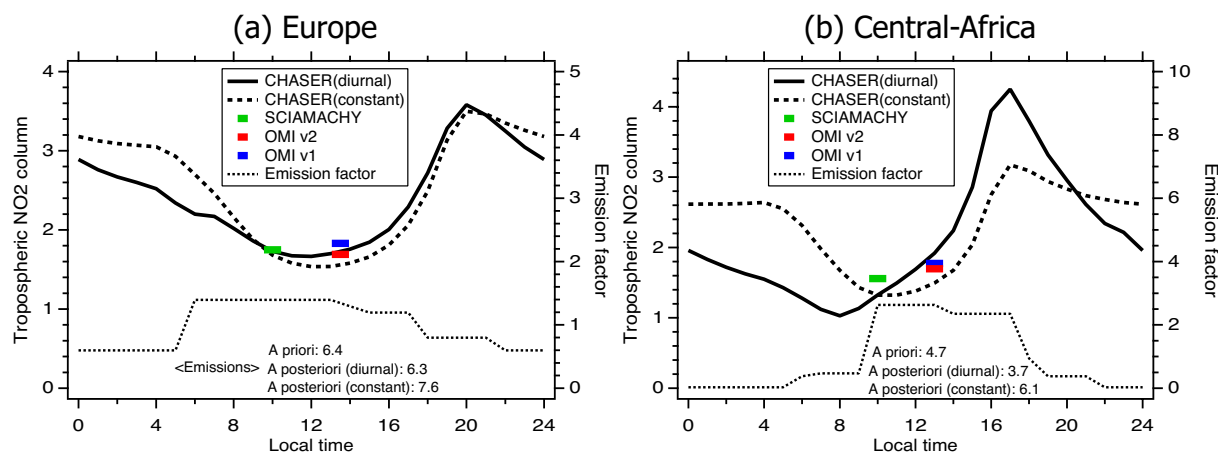
Fig. 4. Monthly mean diurnal variation of tropospheric NO$_2$ columns (in 10^{15} molec. cm^{-2}) obtained from the CHASER simulation with (solid line) and without (broken line) the diurnal variability scheme for surface NO$_x$ emissions over **(a)** Europe (10° W–30° E, 35–60° N) and **(b)** central Africa (10–40° E, 20° S–Equator) in July 2005. Tropospheric NO$_2$ columns obtained from the satellite retrievals: DOMINO v1 (blue), DOMINO v2 (red), and SCIAMACHY (green) are also plotted. The dotted line represents the diurnal variability factor used for NO$_x$ emissions.

data with a reduced random error (e.g. than the individual observation) and results in systematic and smaller analysis increments. Furthermore, the super-observation approach reduces the computational cost of the data assimilation, by reducing the number of data processed in the analysis step.

4.2 Sensitivity to assimilation parameters

Various factors affect the performance and the computational cost of the data assimilation. We have conducted sensitivity experiments to obtain an optimal setting for the data assimilation, as summarized in Table 2. First, the analysis is sensitive to the localization length. The lifetime of NO$_x$ in the lower troposphere varies from several hours to a day, with a longer lifetime during winter than during summer. In addition, long-range transport of, for instance, peroxyacetyl nitrate (PAN) can propagate local NO$_x$ source information to remote places. As a result, the NO$_x$ emission and NO$_2$ concentration will have long distance correlations in some cases. Remote observations will not affect the analysis if the localization length is short, while the analysis will suffer from serious sampling errors by using a too long localization length in combination with a small ensemble size. The optimal localization length was found to be 450 km for the global analysis in January. The optimal length may depend on the location and season because of changes in the NO$_2$ lifetime and wind patters. Second, a large ensemble size is essential to capture background error covariance structures properly, but also increases the computational cost. The analysis improved by increasing the ensemble size to 32, whereas it did not vary significantly by increasing it further. Thus, ensemble size of 32 was preferred to remove sampling errors. Finally, the use of the covariance inflation (cf. Eq. 4) slightly improved

Table 2. The performance of the data assimilation for different parameters: the horizontal localization length (loc in km), the covariance inflation (inf in %), and the ensemble number (num). Five-day mean (averaged over 7–11 January 2005) tropospheric NO$_2$ columns from the assimilation and from DOMINO v2 are compared. Corr is the global spatial correlation coefficient and RMSE is the root-mean-square error in 10^{15} molec. cm^{-2}. The control (CTL) simulation was conducted with loc = 450, inf = 5, and num = 32.

	Corr	RMSE
CTL	0.906	0.599
loc = 300	0.906	0.600
loc = 600	0.897	0.625
loc = 750	0.885	0.645
loc = 900	0.879	0.655
num = 16	0.897	0.612
num = 48	0.906	0.597
num = 64	0.905	0.597
inf = 0	0.904	0.605
inf = 10	0.904	0.607
inf = 15	0.905	0.589

the analysis together with the conditional covariance inflation (cf. Sect. 2.3.2), since it reduces the underestimation in the background error covariance. Although there is no clear optimal value, we employ 5 % covariance inflation.

The performance of the tropospheric NO$_2$ column data assimilation with the optimized settings was evaluated from the χ^2 test (e.g. Ménard and Chang, 2000; Zupanski and Zupanski, 2006). The χ^2 is estimated from the ratio of the

actual OmF to the estimated background covariance. For this test, the innovation statistics are diagnosed from the OmF $\left(\mathbf{y}^o - H\left(\mathbf{x}^b\right)\right)$, the estimated error covariance in the observational space $\left(\mathbf{HP}^b\mathbf{H}^T + \mathbf{R}\right)$, and the number of observations, m.

$$\mathbf{Y} = \frac{1}{\sqrt{m}}\left(\mathbf{HP}^b\mathbf{H}^T + \mathbf{R}\right)^{-1/2}\left(\mathbf{y}^o - H\left(\mathbf{x}^b\right)\right). \tag{14}$$

Using this statistics, the χ^2 is defined as follow:

$$\chi^2 = \text{trace}\,\mathbf{Y}\mathbf{Y}^T, \tag{15}$$

where H is the non-linear observational operator and the $\mathbf{H}$ is the linearization of the observation operator. The mean values of the χ^2 indicate that optimized system is generally within 30 % difference from the ideal value of 1 (Fig. 5). The mean positive bias of the χ^2 is reduced through data assimilation cycles, indicating that the data assimilation tends to provide the optimal solution. The remaining mean positive bias of the χ^2 value ($\sim$25 %) indicates a persistent underestimation of the forecast error variance. The magnitude of the underestimation varied largely with time and space. Although the conditional covariance inflation to the emissions acted to amplify the forecast spread of the tropospheric NO$_2$ column, the adaptive covariance inflation technique (e.g. Anderson, 2009) may help to more properly introduce the inflation to the emissions.

5 Data assimilation results

5.1 Analyzed NO$_x$ emissions

The surface NO$_x$ emissions obtained from the assimilation of DOMINO v2 data for four months in different seasons are shown in Fig. 6 and Fig. 7, and summarized in Table 3. The monthly mean optimized NO$_x$ global source is up to 12 % higher than the a priori emission. Regional differences are more obvious, with a factor of up to about 2.5. The analysis increment is generally positive over eastern China, North America, Australia, northern India, and southern Africa. These positive increments are consistent with the general underestimation of tropospheric NO$_2$ columns in CHASER, consistent with the results by van Noije et al. (2006). An obvious increment is observed over eastern China, with a factor of up to about 1.7 with maxima in January and July, implying that REAS 1.1 (the a priori) largely underestimates the NO$_x$ emissions over eastern China in 2005, as commonly revealed by Kurokawa et al. (2009), but for different years. Part of this underestimation may be attributed to the assumed linear trend in the a priori emissions calculated based on variations between 1995 and 2000 (cf. Sect. 2.2). As shown in Fig. 7, the bottom-up emissions obtained from the newer inventories (EDGAR ver. 4.1, GFED ver. 3.1, and GEIA) are larger than the a priori emissions (REAS 1.1) and are close to the a
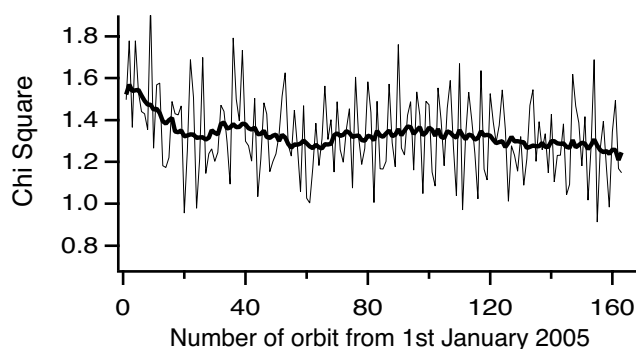

Fig. 5. Temporal variation of the χ^2 calculated as values estimated in each data assimilation cycle (thin line) and 15-orbit cycle running means (bold line).

Table 3. The four-month mean (January, April, July, and October in 2005) global and regional NO$_x$ emissions (in TgN yr^{-1}) obtained from the a priori emissions, the a posteriori emissions with DOMINO v2 data, and the newer inventories (EDGAR4.1+GFED3.1+GEIA).

	A priori	A posteriori
E-China	3.1	5.0
Europe	5.5	4.6
E-USA	2.6	3.4
S-America	0.7	1.1
N-Africa	3.1	2.6
C-Africa	2.0	1.9
S-Africa	0.2	0.5
SE-Asia	0.4	0.7
Northern Hemisphere (20–90° N)	27.1	29.3
Tropics (20° S–20° N)	11.9	12.0
Southern Hemisphere (20–90° S)	2.7	4.1
Globe	41.6	45.4

posteriori emissions over eastern China. However, the wintertime and summertime maxima are not reproduced by both the a priori the newer inventories. The analysis increment also shows significant spatial variations within the regional domains. The estimated emissions are higher than the a priori emissions around large cities in eastern Asia, such as Beijing, Tianjin, Nanjing, Hong Kong, Seoul, and Osaka, whereas it is lower in most remote areas (upper panels in Fig. 8). Consequently, differences in NO$_x$ emissions between large cities and underdeveloped areas generally become larger for the a posteriori emissions than the a priori emissions in eastern Asia.

Over the eastern United States, both the a priori and newer emission inventories are significantly lower than the estimated emissions. The EPA 2005 National Emission Inventory (NEI-05) (U.S. EPA, 2009) showed a larger decrease in anthropogenic NO$_x$ emissions for the United States in
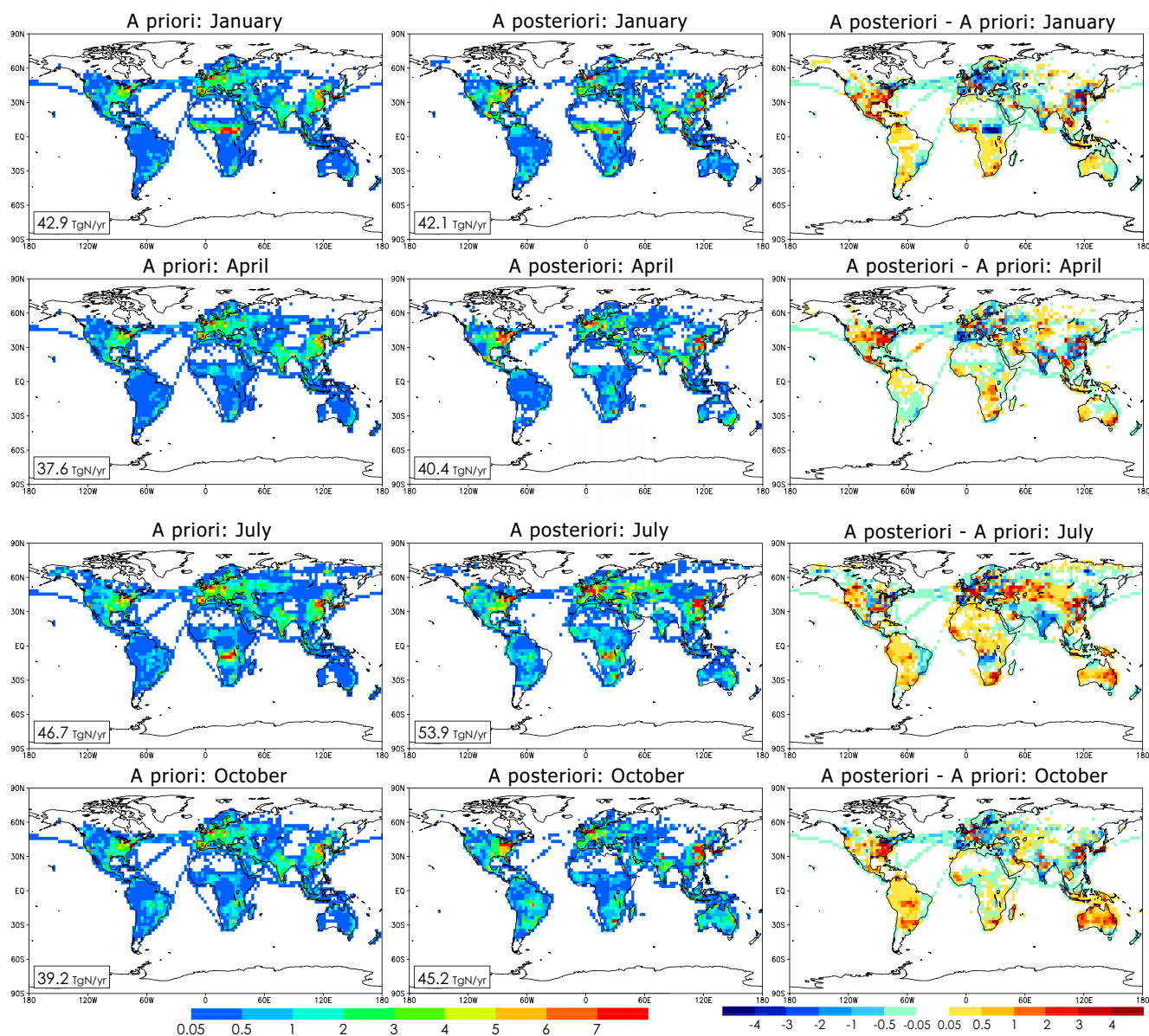
Fig. 6. Global distributions of the surface NO$_x$ emissions (in kg m^{-2} s^{-1}), averaged over the 16–30th of each month, obtained from the a priori emissions (left columns), the a posteriori emissions (the data assimilation results, center columns), and the difference between them (the a posteriori emissions minus the a priori emissions, right columns) in January, April, July, and October 2005. The red (blue) colour in the left and center panels indicates relatively high (low) values. The red (blue) colour in the right panels indicates that the data assimilation increases (decreases) the surface NO$_x$ emissions.

2000–2005 (-15.3 %) than in 1995–2000 (-9.0 %); this appears to be inconsistent with the positive increment obtained for 2005 in this study from the a priori emissions created based on 1995–2000 trends. However, we found that although the trend in 1995–2000 is similar between the a priori emissions (-8.5 %) and the EPA NEI-05 (-9.0 %), the absolute value is 20–30 % lower in the a prior emissions. As a result, the a priori emissions obtained for 2005 over the United States (5.32 TgN yr^{-1}) are lower than the EPA NEI-05 (6.23 TgN yr^{-1}, for this estimates we used the emis-

sion ratio between anthropogenic, soil, and biomass burning emissions over the United States estimated from Zhang et al. (2012)), whereas the a posteriori emissions of 6.90 TgN yr^{-1} are even higher than the EPA NEI-05. The a posteriori emissions reveal higher emissions from autumn to spring than during summer, which differs from the seasonal variation of the a priori emissions. In contrast, the a posteriori NO$_x$ emissions over the contiguous United States are maximized in summer with a July/January ratio of 1.2, consistent with the analysis of NO$_x$ emissions inventories, including the EPA
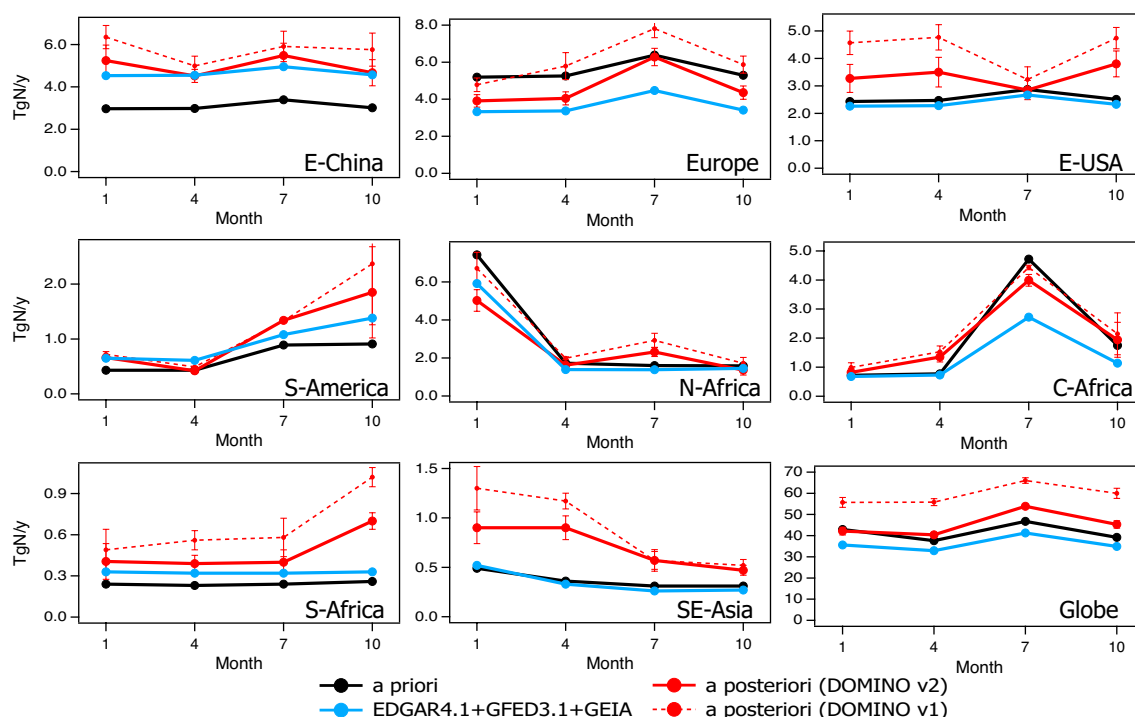
Fig. 7. Seasonal variations of the regional and global surface NO$_x$ emissions (in TgN yr^{-1}) obtained from the a priori emissions (black lines), the a posteriori emissions with DOMINO v2 data (red solid line) and DOMINO v1 data (red dotted line), and the newer inventories (EDGAR4.1+GFED3.1+GEIA, light blue lines), averaged over the 16th-30th of each month in January, April, July, and October 2005. The error bars represent the standard deviations of the a posteriori emissions during the analysis period. The results are shown for eastern China (top left panel), Europe (top center panel), the eastern United States (top right panel), South America (middle left panel), northern Africa (middle center panel), central Africa (middle right panel), southern Africa (bottom left panel), and Southeast Asia (bottom center panel), and the globe (bottom right panel).

NEI-05, soil emissions from Yienger and Levy (1999), and GFED ver. 2, performed by Zhang et al. (2012). Within the eastern United States domain (lower middle panels in Fig. 8), the annual mean a posteriori emissions show higher values than the a priori emissions around large cities in the eastern United States; e.g. around Chicago, Indianapolis, Atlanta, and the Florida peninsula. In contrast, the a posteriori emissions are smaller in the northern part of North America (e.g. around Montreal and Toronto), as well as around Houston, with factors of less than 0.6 being observed. A large increase in NO$_x$ emissions also appears in the Highveld region of southern Africa, with a factor of about 1.7 in October.

Different from other industrial areas, the a posteriori emissions are lower than the a priori emissions over Europe, except during summer, and the newer inventories are lower than both the a priori and the a posteriori emissions. Both the a priori and a posteriori emissions reveal maximum emissions in summer, but the seasonal amplitude is about 15 % higher for the a posteriori emissions over Europe. The increment is mostly positive over northwestern Europe, including Germany, France, Switzerland, and southern England, whereas it is negative over southwestern and Eastern Europe (upper middle panels in Fig. 8). It should be noted that the linear

temporal extrapolation (based on the 1995 and 2000 inventories, see Sect. 2.2) may give spurious results for certain regions. For instance, the a priori emissions in Spain are unrealistically high, and are strongly reduced by the assimilation. They contributed significantly to the European mean.

The seasonal variations in biomass burning emissions may vary greatly with year, while the data assimilation corrects the timing and the strength of emissions from biomass burning for the analysis year. Over central Africa, the a posteriori emissions are larger than the a priori emissions in April (with a factor of 2), and smaller in July (with a factor of 0.85), reflecting observed seasonal variations in biomass burning activity (e.g. Fig. 3). As a result, the seasonal amplitude of the central African emissions in 2005 becomes smaller in the a posteriori than the a priori emissions. Over northern Africa, the data assimilation decreases the emissions in January with a factor of 0.7, but increases the emissions in July with a factor of 1.4. Although the annual mean a priori and a posteriori emissions values are similar over northern Africa, the spatial distribution is largely modified. The assimilation decreases the emissions in the eastern part of the northern Africa, but increases the emissions in the western part of northern Africa (lower panels in Fig. 8). Over
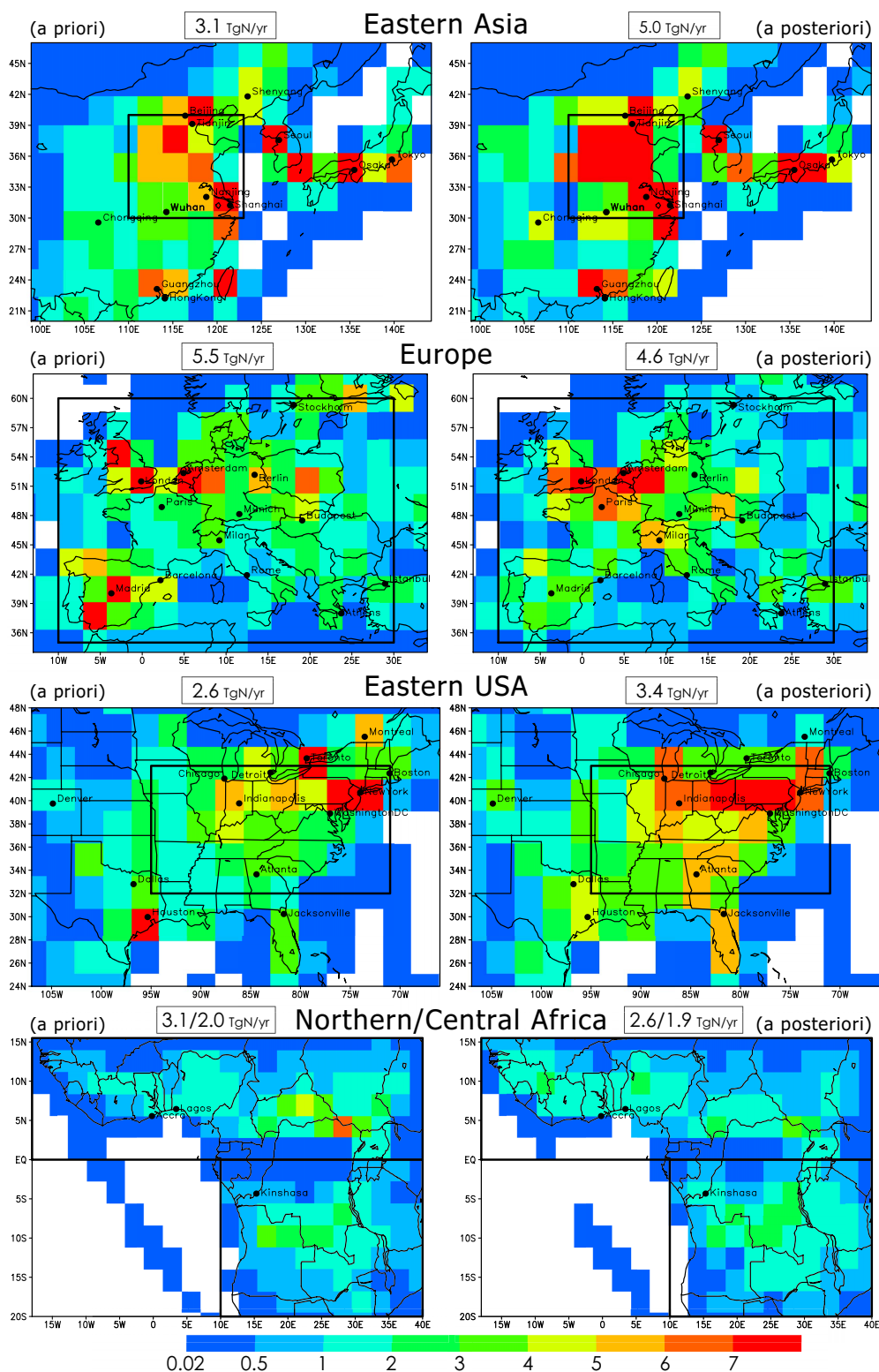
Fig. 8. Same as Fig. 6, but showing the regional distribution over eastern Asia (upper panels), Europe (upper middle panels), the eastern United States (lower middle panels), and central Africa (lower panels), obtained from the a priori emissions (left panels) and the a posteriori emissions (right panels), averaged over four months, January, April, July, and October, in 2005. The black square line represents the region used for the regional mean analysis; the number shown in the top of the panels represents the total NO$_x$ emission for the regional domain. The red (blue) colour indicates relatively high (low) values.

Southeast Asia, the data assimilation greatly increases NO$_x$ emissions, with a largest (a factor of 2.5) increase in April. Over South America, a large increase occurs in October (a factor of 2), reflecting the high concentration observed over the Amazon (monthly mean concentration greater than 2×10^{15} molec. cm^{-2}), which is probably a result of forest fires and was not reproduced by the a priori emission. Accordingly, the estimated emissions over Southeast Asia and South America have a maximum value in spring, while the maximum a priori emissions occur during winter (Fig. 7). The data assimilation may also capture signals related to soil emissions, for which the inventories may have large uncertainties. For example, the regional mean emissions over Australia are increased by a factor of 1.2–1.4 with a maximum increase in October. The emissions are also increased over central China (Fig. 6). These positive increments may indicate the underestimation of soil emissions in the a priori emission.

By assimilating DOMINO v2 data, NO$_x$ emissions from ships mostly become smaller than the a priori emissions. The negative increment may indicate an overestimation of ship emissions in the a priori. The negative increment can also be largely influenced by an underestimation of tropospheric NO$_2$ columns in the retrieval. Boersma et al. (2008b) found that DOMINO v1 data generally have lower columns with a mean bias of 0.6×10^{15} molec. cm^{-2} over the ocean when compared to aircraft measurements during the INTEX-B campaign. The difference in tropospheric NO$_2$ columns between DOMINO v1 and v2 data are generally very small over the ocean (Boersma et al., 2011), which suggest a similar bias for v2 compared to INTEX-B data. The errors in stratospheric NO$_2$ columns could also cause errors in tropospheric NO$_2$ column retrievals over oceans (Lamsal et al., 2010). Alternatively, the data assimilation system may have difficulties in correcting weak emissions, because of the treatment of the analysis spread (cf. Sect. 2.3.2) and large observation errors. Also, the fast chemical processing in the exhaust plume of the ship is a process that is not resolved by the CTM.

As summarized in Table 3, the data assimilation increased the annual (four-month) mean NO$_x$ emissions by about 8 % in the Northern Hemisphere (20–90° N) and by about 50 % in the Southern Hemisphere (20–90° S). The impact on the tropical total emission is small. The estimated annual mean global NO$_x$ emissions of 45.4 TgN yr^{-1}, increased by about 9 % from the a priori, is somewhat larger than that estimated from previous studies (e.g. 42.1 TgN yr^{-1} (Müller and Stavrakou, 2005), 37.8 TgN yr^{-1} (Martin et al., 2003), 40.3 TgN yr^{-1} (Jaeglé et al., 2005)). In the regional scale, the a priori emissions estimated from this study generally show agreement with other top-down studies. The 0.465 TgN estimated over the Eastern United States (102–64° W, 22–50° N) from the OMI observations for March 2006 (Boersma et al., 2008a) is comparable to our estimate of 0.500 TgN for the same period. The 0.73 TgN estimated over the United States (130–70° W, 25–50° N) from ICARTT observations

for 1 July–15 August 2004 (Hudman et al., 2007) is slightly smaller than our estimates of 0.98 TgN for July 2005. The 7.72 TgN (8.0 TgN) estimated for July 2008 (January 2009) over east China (103.75–123.75° E, 19–45° N) from OMI and GOME-2 observations (Lin and McElroy, 2010) is comparable to our estimates of 7.8 TgN (6.5 TgN) for July 2005 (January 2005). The 11.0 TgN yr^{-1} estimated over East Asia (80–150° E, 10–50° N) for July 2007 from OMI observations (Zhao and Wang, 2009) is comparable to our estimates of 11.8 TgN yr^{-1} for July 2005. Differences in analysis years, together with those in retrieval data and models used in the analysis, will primarily contribute to the difference in NO$_x$ emission estimates (e.g. Jaeglé et al., 2005). This will be further discussed in Sect. 6.

5.2 Validation with satellite data

As illustrated in Fig. 9 and summarized in Table 4, the assimilation run shows a better agreement with the satellite retrieval than the model simulation for most areas. When compared with the OMI data, the spatial correlation of the global NO$_2$ distribution becomes 0.04–0.19 higher, and the global mean RMSE is decreased by 25–40 % by the data assimilation. The improvement is commonly observed even when compared with independent SCIAMACHY data, with an increase in the global spatial correlation of about 0.03–0.10 and a decrease in the global mean RMSE of about 10–25 %. As an exception, the global mean bias compared to the SCIAMACHY is not improved by the data assimilation, likely because of the systematic bias between the SCIAMACHY and the assimilated data (DOMINO v2, cf. Sect. 3.1); that is, the mean concentration over land is smaller in the DOMINO v2 data than in the SCIAMACHY retrieval.

The regional mean tropospheric NO$_2$ columns are compared in Table 5. The negative bias of the model is largely reduced over most industrial areas by the data assimilation, especially over eastern China, Europe, southern Africa, and the eastern United States. For example, the data assimilation removes the negative bias when compared to the OMI (SCIAMACHY) retrieval by about 80–90 (60–80) % over eastern China. The negative bias is also largely removed over the eastern United States. The persistent negative bias over Australia and southern Africa is also largely reduced by about 10–50 %. Over Europe, the data assimilation reveals large reductions in the positive bias in January. Improvements are also observed over biomass burning areas. Obvious negative biases of the model over South America in spring and over Southeast Asia in spring-autumn are mostly (more than 65 %) removed by the data assimilation. These improvements are commonly observed even when compared with the independent SCIAMACHY data.

Because of the effective corrections in NO$_x$ emissions by the data assimilation, the OmF distributions of the tropospheric NO$_2$ columns narrows, and its mean value (i.e. bias) becomes smaller (Fig. 10). For instance, the standard

Table 4. Comparisons of tropospheric NO$_2$ columns between the data assimilation run and the satellite retrievals DOMINO v2 (OMI) and SCIAMACHY (SCIA). The results are obtained from 15-day averages (from the 16th to the 30th of each month) provided for four months in 2005. Shown are the global spatial correlation (Corr), the root-mean-square error (RMSE), and the mean bias in 10^{15} molec. cm^{-2}. The model simulation results (without data assimilation) are also shown in brackets.

|		January	April	July	October
vs. OMI	S-Corr	0.92 (0.73)	0.93 (0.87)	0.93 (0.89)	0.95 (0.86)
	RMSE	0.50 (0.82)	0.28 (0.38)	0.23 (0.30)	0.29 (0.45)
	Bias	0.01 (−0.01)	0.02 (−0.02)	0.00 (−0.04)	−0.03 (−0.07)
vs. SCIA	S-Corr	0.87 (0.77)	0.84 (0.81)	0.81 (0.76)	0.86 (0.77)
	RMSE	0.85 (1.11)	0.54 (0.60)	0.52 (0.58)	0.49 (0.61)
	Bias	−0.01 (−0.06)	0.14 (0.09)	0.08 (0.04)	0.10 (0.06)

Table 5. The 15-days mean (averaged over the 16–30th of each month) bias of regional mean tropospheric NO$_2$ columns; the data assimilation run minus the satellite retrievals (DOMINO v2 (OMI) and SCIAMACHY (SCIA)) in 10^{15} molec. cm^{-2}, for four months in 2005. The model simulation results (without data assimilation) are also shown in brackets.

		January	April	July	October
E-China	vs. OMI	−0.67 (−4.58)	−0.19 (−1.64)	−0.08 (−0.78)	−0.53 (−2.42)
	vs. SCIA	−1.37 (−7.24)	−0.64 (−2.54)	−0.77 (−1.93)	−1.09 (−2.85)
Europe	vs. OMI	−0.12 (0.84)	−0.40 (−0.35)	−0.09 (−0.26)	−0.31 (−0.25)
	vs. SCIA	−0.58 (0.08)	−0.21 (−0.11)	0.07 (−0.04)	0.29 (0.36)
E-USA	vs. OMI	−1.92 (−2.65)	−0.96 (−1.68)	−0.04 (−0.31)	−0.52 (−1.46)
	vs. SCIA	−4.79 (−5.40)	−0.92 (−1.85)	−0.23 (−0.52)	−0.78 (−1.63)
S-America	vs. OMI	0.02 (−0.03)	0.05 (0.02)	−0.06 (0.10)	0.03 (−0.43)
	vs. SCIA	0.09 (0.05)	0.54 (0.49)	0.03 (0.15)	−0.02 (−0.43)
N-Africa	vs. OMI	0.12 (0.15)	0.11 (−0.07)	−0.11 (−0.22)	−0.04 (0.05)
	vs. SCIA	−0.07 (−0.07)	0.21 (0.19)	−0.12 (−0.21)	0.18 (0.29)
C-Africa	vs. OMI	−0.17 (−0.25)	0.13 (−0.05)	−0.19 (−0.27)	−0.37 (−0.50)
	vs. SCIA	−0.22 (−0.31)	0.30 (0.02)	−0.48 (−0.54)	−0.33 (−0.43)
S-Africa	vs. OMI	−0.54 (−0.73)	−1.17 (−1.42)	−1.58 (−2.80)	−0.74 (−1.38)
	vs. SCIA	−2.16 (−2.47)	−2.74 (−3.02)	−3.42 (−4.73)	−0.54 (−1.79)
SE-Asia	vs. OMI	−0.01 (−0.32)	−0.14 (−0.44)	0.16 (−0.09)	−0.09 (−0.15)
	vs. SCIA	0.24 (−0.21)	−0.29 (−0.54)	0.18 (0.16)	0.19 (0.17)

deviations of the OmF and the mean bias become about 30 % and 90 %, respectively, smaller by the data assimilation over Europe. Also, a large improvement over eastern China is related to the reduction of the negative model bias, or OmF values larger than 5 ×10^{15} molec. cm^{-2}.

Although the persistent model bias is largely removed by the emission correction, there are still large disagreements between the simulated and observed NO$_2$ columns in some areas. The quality and the abundance of the OMI retrieval vary largely with season and area, reflecting observation conditions (e.g. clouds, aerosols, and surface albedo), as summarized in Table 6. The observation does not effectively correct the model state when the observation error is large compared to the background error. Insufficient improvements by the

data assimilation can be attributed to a large observation error and small amounts of observations for some regions. This occurs over Europe in April and October (large errors), over the eastern United States in January (small number of observations), over South America in January and April (large errors and small number of observations), over northern Africa in April (large errors), and over southern Africa in January (small number of observations). In addition, the data assimilation run was conducted from the beginning of each month (for a month) starting from the a priori emission. A continuous run over a few months may further improve the analysis by accumulating observational information with time, although the computational cost becomes high. The agreement between the simulated and observed NO$_2$ fields may
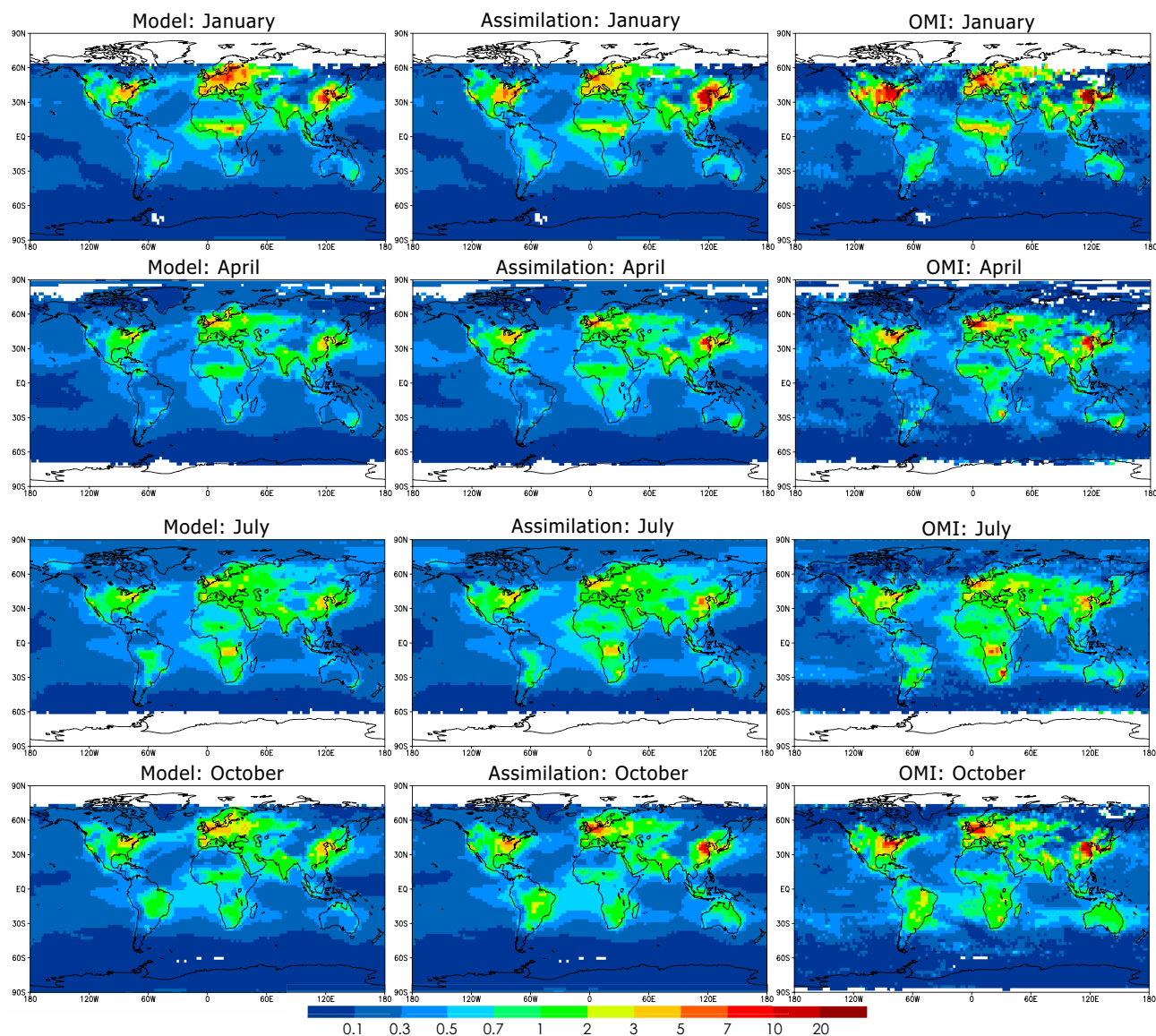
Fig. 9. Global distributions of the tropospheric NO$_2$ columns (in 10^{15} molec. cm^{-2}), averaged over the 16–30th of each month, obtained from the CHASER simulation (w/o data assimilation, left columns), the data assimilation run (center columns), and DOMINO v2 (right columns) in January, April, July, and October 2005. The red (blue) colour indicates relatively high (low) values.

be further improved by a more realistic diurnal variability scheme especially over biomass burning regions (e.g. over central Africa; cf. Sects. 3.3 and 6).

Unlike the mean bias reduction, the data assimilation did not improve the temporal correlation significantly (figure not shown). The data assimilation accumulates observational information with time and gradually changes the emissions reflecting the OmF, the background spread, and the observation error. To reproduce rapid changes in concentrations, more constraints from observations and larger inflation to the background spread (cf. Sect. 2.3.2) are required. Meanwhile, the analysis increments are also sensitive to the error correlation assumed in the super observation (e.g. Sect. 2.3.3).

5.3 Validation with profile data

Figure 11 shows a comparison of the vertical profiles of the model simulation, the data assimilation analysis, and the aircraft observations during the INTEX-B campaign. High NO$_2$ concentrations are observed in the boundary layer at pressures higher than 950 hPa in the morning (08:00–10:00 a.m.) up to 5 parts per billion by volume (ppbv), and at pressures higher than 900 hPa in the afternoon (02:00–04:00 p.m.) up to 0.6 ppbv. The lower concentration in the afternoon is mainly caused by chemical loss through the reaction with OH and vertical mixing in the planetary boundary layer (PBL) during day time. Both in the morning and in the afternoon,
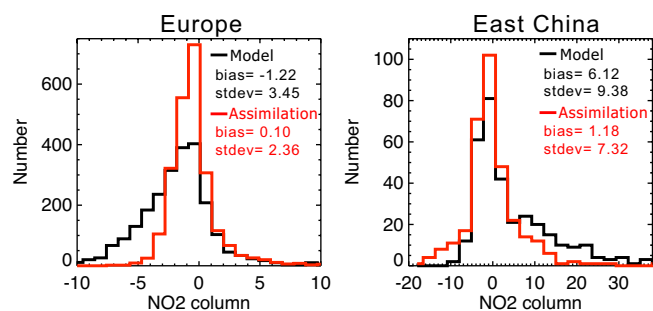
Fig. 10. Observation minus forecast (OmF) distributions of tropospheric NO$_2$ columns (in 10^{15} molec. cm^{-2}) calculated from the model simulation (black line) and the data assimilation run (red line) over Europe (10° W–30° E, 35–60° N, left panel) and eastern China (110–123° E, 30–44° N, right panel) for the period 16–30 January 2005. The numbers shown in the figures are the mean value (bias) and the standard deviation (stdev) of the OmF in 10^{15} molec. cm^{-2} for the model simulation (black) and for the assimilation run (red).

Table 6. The 15-day mean (16–30th of each month) and regional mean relative observation error for DOMINO v2. The relative error was estimated by dividing the mean observation error by the mean observation concentration for each super-observation. The mean number of OMI pixels (per day per $1.0° \times 1.0°$) used for making the super-observation is shown in brackets. Note that during the calculation of the relative error, 0.1×10^{15} molec. cm^{-2} was added to both the denominator and the numerator to avoid the divergence caused by near-zero concentrations and to reduce the influence of remote site data.

	January	April	July	October
E-China	1.1 (8.6)	0.9 (17.0)	0.5 (9.2)	1.0 (14.3)
Europe	1.1 (9.8)	1.5 (13.7)	1.0 (15.6)	1.5 (15.0)
E-USA	0.7 (10.5)	0.9 (13.4)	0.5 (17.3)	0.9 (16.5)
S-America	1.5 (5.4)	2.0 (6.2)	1.6 (20.5)	1.2 (7.9)
N-Africa	1.2 (22.7)	1.4 (17.2)	0.9 (15.9)	1.2 (20.2)
C-Africa	1.3 (10.8)	1.5 (14.9)	0.9 (19.7)	0.8 (10.1)
S-Africa	1.0 (6.3)	1.0 (13.6)	0.9 (25.5)	0.8 (15.9)
SE-Asia	1.0 (24.4)	0.9 (16.1)	1.9 (2.9)	1.3 (11.1)

the lowest part of the profile is well reproduced by the data assimilation run, whereas the model simulation underestimates it by about 30–40 %. The assimilation of DOMINO v2 (DOMINO v1) revealed a significant increase in surface NO$_x$ emissions by a factor of about 1.3–1.6 (1.6–1.9) around Mexico. Boersma et al. (2008b) showed a similar increase in NO$_x$ emissions in their top-down estimate using DOMINO v1 data by a factor of about 2.0 for Mexico. Above the PBL, the NO$_2$ concentrations decrease with height, mainly due to he relatively short lifetime of the NO$_x$ family. Both the model and assimilation run have lower NO$_2$ concentrations with differences of up to 0.1 ppbv when compared to the observed value in the free troposphere. This discrepancy may be attributed to errors in the model, such as too much chemical loss of NO$_2$, too small lightning productions, unrealistic representations of the NO$_y$ species partitioning, and atmospheric transport.

The comparison with lidar profiles obtained during the DANDELIONS campaign is shown in Fig. 12. Cabauw is surrounded by major populated areas within a distance of a few 100 km, and the model grid concentration is considered to be representative for the observation data. Both the simulated and the observed values show a rapid decrease in NO$_2$ concentrations within the PBL from the surface to about 600 m (Fig. 12a). The assimilation improves the amount of NO$_2$ in the boundary layer, but provides concentrations that are too high near the surface. The grid cells used for the interpolation to the Cabauw tower partially cover the North Sea, and have very different boundary layer heights, which may explain the concentration gradient in the model profiles. A positive intercept near the ground surface indicates that the model has problems representing the measurement location. The near-surface concentration will be sensitive to the model resolution owing to fine-scale emission distribu-

tion and transport. The scatter plots (Fig. 12b, c) demonstrate that the data assimilation also improves the variability of the NO$_2$ concentration especially below 500 m. The slope is 0.46 in the case of the model simulation, whereas it is much larger (0.99) in the data assimilation run. The assimilation does not change the model profile in the free troposphere.

Changes in the NO$_x$ fields affect the concentrations of various chemical species through chemical processes during the forecast step. The impact on ozone is analyzed for the INTEX-B campaign at Mexico City, by comparing simulated O$_3$ fields with vertical O$_3$ profiles measured from the ozone sonde. Figure 11c shows that the assimilation of OMI NO$_2$ data reduces the discrepancy in O$_3$ concentrations between the model and observations for the lower troposphere. The enhanced NO$_x$ emissions by the data assimilation increase chemical production of O$_3$. Thus, NO$_x$ emissions updated by the data assimilation have the potential to improve the ozone chemistry in the model, although its impact on the free tropospheric ozone is not obvious in this case. The free tropospheric ozone is too low by about 10 parts per trillion by volume (pptv) in both the simulation and the assimilation. An underestimation of nearly 10 pptv was commonly observed for a GEOS-Chem model simulation over the United States during the International Consortium on Atmospheric Transport and Transformation (ICARTT) aircraft campaign (Hudman et al., 2007). Hudman demonstrated that an enhanced lightning NO$_x$ source (0.27 TgN over the United States from 1 July to 15 August 2004) removed most of the upper tropospheric ozone bias in their standard simulation (which had only 0.068 TgN from lightning). The similar magnitude of the ozone underestimation and lightning source (0.061 TgN) in our CHASER simulation shows that although the global total lightning source is similar for
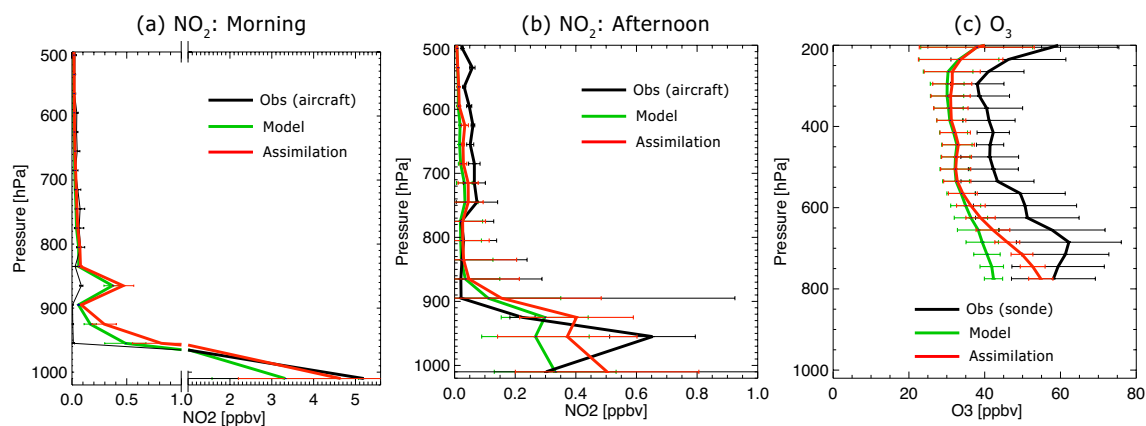
Fig. 11. Vertical profiles of the NO$_2$ concentrations (in ppbv) in **(a)** the morning (08:00 a.m.–10:00 a.m.) and **(b)** the afternoon (02:00 p.m.–04:00 p.m.) and **(c)** the O$_3$ concentrations (in ppbv) obtained during the INTEX-B campaign in March 2006. The black lines represent the observed profile; the green lines represent the model simulation; the red line represents the data assimilation run. The error bars represent the standard deviation of all the data within one grid cell.
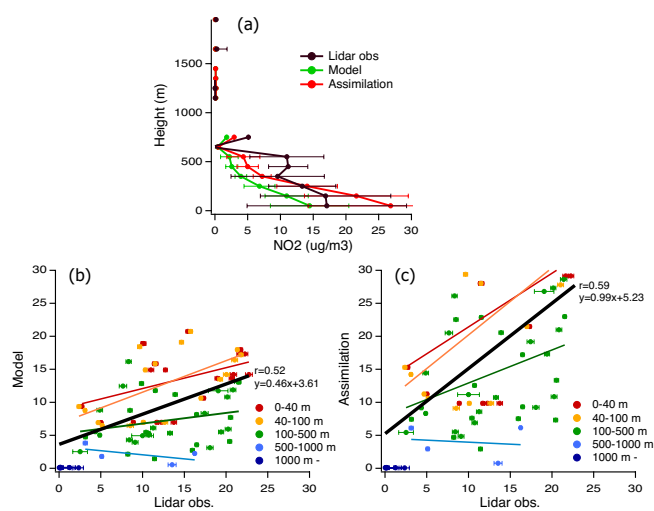
Fig. 12. **(a)** Mean vertical profiles of the NO$_2$ concentrations (µg m^3) obtained during the DANDELIONS campaign in September 2006. The black lines represent the lidar observation; the green lines represent the model simulation; the red line represents the data assimilation run. The error bars represent the standard deviation of all the data within one grid. Lower panels show scatter plots of NO$_2$ concentrations (µg m^3) for **(b)** the model simulation and **(c)** the data assimilation run during the DANDELIONS campaign. The straight lines represent linear regression lines for each level. Each line represents a linear fit to the points of the same colour, and the colours represent the altitude level. The black line shows a linear fit to all of the data.

our simulation (7.5 TgN yr^{-1}) and estimates from chemical observations (mostly 6–8 TgN yr^{-1}) (e.g. Martin et al., 2007; Sauvage et al., 2007), CHASER may underestimate lightning NO$_x$ sources and their-induced ozone production in the free troposphere over Mexico and North America. Errors in the

stratospheric ozone transport into the troposphere may also contribute to the ozone underestimation.

6 Sensitivity to the retrieval and model setting

Independent retrievals have different qualities, vertical sensitivities, and overpass times. These differences may result in obvious changes in the emission estimates. In addition, the performance of the model plays an important role in the emission estimates because it provides the relationship between surface fluxes and atmospheric concentrations. Thus, it is important to consider the effects of these factors on the estimated emissions. Here, we investigate the sensitivity of the emission estimates to the retrieval product and model settings. The sensitivities are shown for a season when the sensitivity is largest (Fig. 13); January for the DOMINO 1 and SCIAMACHY data assimilation experiments and July for the lightning NO$_x$ production and the diurnal variability scheme experiments, as described below.

By assimilating DOMINO v1 data instead of DOMINO v2 data, the a posteriori emissions increase by 5–45 % over most areas (Fig. 13). The emission increase corresponds to higher concentrations in DOMINO v1 as compared to DOMINO v2. This difference is obvious in January over eastern China, the eastern United States, Europe, northern Africa, and Southeast Asia. The comparison indicates that errors in the retrieval algorithm lead to large uncertainties in top-down emissions. The assimilation of the SCIAMACHY columns also shows significant differences especially over South America, southern Africa, and Southeast Asia, with relative changes of about 30–80 %. The differences between the emissions estimated using the OMI and SCIAMACHY retrievals can be partly attributed to errors related to the simplified description of the diurnal variability in the model
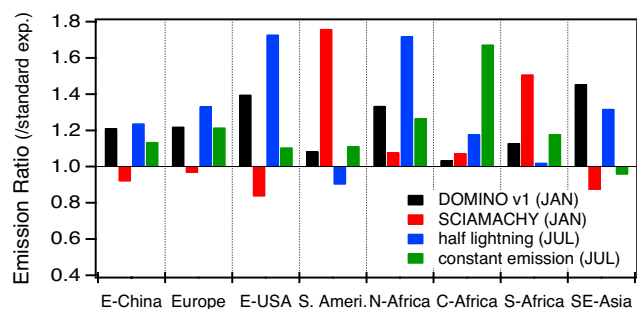
Fig. 13. Ratios of the regional mean NO$_x$ emissions between the standard assimilation experiments using the DOMINO v2 observations and experiments conducted using different satellite products: the DOMINO v1 retrieval (black bars) and the SCIAMACHY retrieval (red bars) in January. Also shown are the emission ratios between the standard assimilation experiments and experiments conducted using different model settings: a 50 % reduction of NO$_x$ emissions by lightning (blue bars) and without the diurnal variability scheme for the surface emissions (green bars) in July. The ratio greater (less) than one indicates that the NO$_x$ emissions are higher (lower) in the sensitivity experiments than in the standard assimilation experiments.

along with systematic differences between the retrievals. We note that the SCIAMACHY and DOMINO v1 products are based on a very similar algorithm, and one could expect a similar behavior for these products compared to DOMINO v2. However, Fig. 13 shows that the emission ratios are quite different in different regions. The difference may be largely attributed to the simplified diurnal variability scheme especially over biomass burning regions. In addition, the poorer spatial and temporal resolutions and less global coverage in the SCIAMACHY retrieval than in the OMI retrieval may also cause the differences.

The bias in NO$_2$ columns is also influenced by NO$_x$ processes in the upper troposphere in remote areas (Napelenok et al., 2008). Boersma et al. (2005) suggested that the contribution of lightning to the tropospheric NO$_2$ column is strongest in the tropics, with a contribution of 0.4 × 10^{15} molec. cm^{-2}. We found that changes in the lightning emissions have a large effect on the estimated NO$_x$ emissions. Specifically, by reducing the global lightning productions by half (from 7.5 to 3.75 TgN), the NO$_x$ emissions increased by about 30–80 % over the eastern United States, northern Africa, and Southeast Asia in July, as similarly demonstrated by Lin et al. (2010). The performance of the mixing scheme may also affect the tropospheric NO$_2$ columns. A too diffusive PBL mixing may result in an underestimation of the NO$_2$ columns because of the reduction in the NO$_2$/NO ratio with height. As demonstrated in Sect. 5.3, the model used shows an underestimation in the free tropospheric NO$_2$ concentration during the INTEX-B campaign. This underestimation may lead to an overestimation of the estimated surface emissions in the data assimilation. Thus, re-

alistic representations of atmospheric processes in the model are required to improve the emissions estimates. Simultaneous optimization of atmospheric (e.g. lightning) and surface NO$_x$ sources will be performed in future studies.

The implementation of the diurnal variability scheme largely influences the emission estimates (cf. Fig. 4). For example, the emission was decreased from the a priori by 22 % over central Africa in the data assimilation with the diurnal variability scheme, whereas it was increased by 30 % in the data assimilation with a constant emission. Similar differences between the experiments with and without the diurnal variation scheme were also found over industrial areas (e.g. over Europe). Although the estimated emission was largely affected by the diurnal variability scheme, the prescribed diurnal variation profile is highly simplified, and it will not accurately represent the temporal variations of emissions. An alternative approach is required to determine the diurnal variability profile from analyses of multiple polar or future geostationary satellite instruments.

7 Conclusions

We have developed an advanced data assimilation system to estimate global NO$_x$ emissions. An ensemble Kalman filter approach was developed, in which the state augmentation method was employed to estimate daily global surface emissions of NO$_x$ with a horizontal resolution of 2.8° using OMI tropospheric NO$_2$ column retrievals. This approach allows us to (1) accumulate observational information with time and (2) reflect the non-direct relationship between the emissions and tropospheric columns because of the use of the background error covariance dynamically estimated from the ensemble of CTM forecasts. A super-observation approach was employed to produce data representative for a model grid cell, which helped improve the assimilation analyses.

The inversion increased the NO$_x$ emissions in eastern China, the eastern United States, southern Africa, and central-eastern Europe, suggesting that the anthropogenic emissions are mostly underestimated in the a priori emissions that were constructed based on bottom-up inventories. An obvious increase in the emission was observed over eastern China, with a factor of up to 1.7. A large increase in NO$_x$ emissions also appears in the Highveld region of southern Africa and over the eastern United States, with a factor of about 1.4–2.5. Different from other industrial areas, the regional mean a posteriori emissions were lower than the a priori emissions over Europe, although the analysis increment showed obvious spatial variations (e.g. mostly positive over northwestern Europe and negative over eastern and southwestern Europe). The data assimilation also corrected the timing and the amplitude of the emissions from biomass burning, with a large increase over central Africa (with a factor of 2) and Southeast Asia (with a factor of 2.5) in April and over South America (with a factor of 2) in October. As a

result, the a posteriori emissions over these biomass burning areas showed the maximum value in spring in the analysis year 2005, which differed from the wintertime maximum for the emission inventories. The estimated emissions are generally more similar to the newer inventories obtained from the EDGAR 4.1, GFED 3.1, and GEIA data sets than the a priori emissions constructed based on older inventories, although there are large discrepancies between the estimated emissions and the newer inventories over Europe, the eastern United States, Central Africa, and Southeast Asia.

The data assimilation results were validated by comparing the simulated NO$_2$ concentrations with independent data: the SCIAMACHY satellite retrieval and vertical profiles obtained during the INTEX-B and DANDELIONS campaigns. The emission correction led to significant reductions in the disagreement between the simulated and observed NO$_2$, suggesting that the data assimilation improves the representation of surface NO$_x$ emissions. The emission correction improved the NO$_2$ profiles within the boundary layer below about 500 m, whereas its impact was small in the free troposphere. Thus, more constraints on the free tropospheric processes (e.g. lightning productions) are required for further improving the vertical distribution of the NO$_x$ sources. Meanwhile, although OMI provides global coverage of NO$_2$ concentrations, the effectiveness of the data assimilation was largely determined by the quality and the frequency of the observation.

Because of various error sources in both the model and the satellite retrieval, there are large uncertainties in the estimated emissions. In fact, the emissions estimates were sensitive to both the retrieval data and the model setting used for the data assimilation. Different retrievals resulted in large discrepancies in the analyzed NO$_x$ emissions. Thus, possible biases in the retrieval seriously degrade the emission analysis, with mean differences up to 60–70 % depending on the region. Furthermore, the observation minus forecast statistics showed significant diurnal variations. As a result of the uncertainty in the retrievals and in the diurnal variability scheme of the model, the use of different satellite products obtained at different overpass times causes large discrepancies in the emission estimates. In addition, the model performance in the upper troposphere (e.g. lightning NO$_2$ production) largely affected the emission estimation. Thus, it is important to consider both the model performance and retrieval dependence for better constraints on the NO$_x$ sources.

In this study, only NO$_2$ data were assimilated to constrain the surface NO$_x$ emissions. Multiple-species (e.g. HNO$_3$ and O$_3$) data obtained from various platforms can provide additional constraints through their chemical interactions. Meanwhile, only total emissions were adjusted from the data assimilation in this study. Sector-specific adjustments may help to explore the change in contributions of each emission source. It is also interesting to investigate the long-term variations of the emissions. Moreover, the surface NO$_x$ emission estimate may be further improved by simultaneous optimiza-

tion of atmospheric (e.g. lightning) and surface NO$_x$ emissions, which impact the vertical distribution of NO$_x$ sources. Advanced chemical data assimilation systems, such as developed by this study, make it possible to combine various data sets and to simultaneously optimize multiple model variables, including the atmospheric distribution of polluting trace gases and their precursor emissions.

References

Aksoy, A., Zhang, F., and Nielsen-Gammon, J. W.: Ensemble-Based Simultaneous State and Parameter Estimation in a Two-Dimensional Sea-Breeze Model, Mon. Weather Rev., 134, 2951–2970, doi:10.1175/MWR3224.1, 2006.

Anderson, J. L.: Spatially and temporally varying adaptive covariance inflation for ensemble filters, Tellus A, 61, 72–83, doi:10.1111/j.1600-0870.2008.00361.x, 2009.

Blond, N., Boersma, K. F., Eskes, H. J., van der A, R. J., van Roozendael, M., De Smedt, I., Bergametti, G., and Vautard, R.: Intercomparison of SCIAMACHY nitrogen dioxide observations, in situ measurements and air quality modeling results over Western Europe, J. Geophys. Res., 112, 1–20, doi:10.1029/2006JD007277, 2007.

Boersma, K. F., Eskes, H. J., and Brinksma, E. J.: Error analysis for tropospheric NO$_2$ retrieval from space, J. Geophys. Res., 109, D04311, doi:10.1029/2003JD003962, 2004.

Boersma, K. F., Eskes, H. J., Meijer, E. W., and Kelder, H. M.: Estimates of lightning NO$_x$ production from GOME satellite observations, Atmos. Chem. Phys., 5, 2311–2331, doi:10.5194/acp-5-2311-2005, 2005.

Boersma, K. F., Eskes, H. J., Veefkind, J. P., Brinksma, E. J., van der A, R. J., Sneep, M., van den Oord, G. H. J., Levelt, P. F., Stammes, P., Gleason, J. F., and Bucsela, E. J.: Near-real time retrieval of tropospheric NO$_2$ from OMI, Atmos. Chem. Phys., 7, 2103–2118, doi:10.5194/acp-7-2103-2007, 2007.

Boersma, K. F., Jacob, D. J., Bucsela, E. J., Perring, A. E., Dirksen, R., van Der A, R. J., Yantosca, R. M., Park, R. J., Wenig, M. O., Bertram, T. H., and et al.: Validation of OMI tropospheric NO$_2$ observations during INTEX-B and application to constrain NO$_x$ emissions over the eastern United States and Mexico, Atmos. Environ., 42, 4480–4497, doi:10.1016/j.atmosenv.2008.02.004, 2008a.

Boersma, K. F., Jacob, D. J., Eskes, H. J., Pinder, R. W., Wang, J., and van der A, R. J.: Intercomparison of SCIAMACHY and OMI tropospheric NO$_2$ columns: Observing the diurnal evolution of chemistry and emissions from space, J. Geophys. Res., 113, 1–14, doi:10.1029/2007JD008816, 2008b.

Boersma, K. F., Eskes, H. J., Dirksen, R. J., van der A, R. J., Veefkind, J. P., Stammes, P., Huijnen, V., Kleipool, Q. L., Sneep,

M., Claas, J., Leitão, J., Richter, A., Zhou, Y., and Brunner, D.: An improved tropospheric NO$_2$ column retrieval algorithm for the Ozone Monitoring Instrument, Atmos. Meas. Tech., 4, 1905–1928, doi:10.5194/amt-4-1905-2011, 2011.

Bovensmann, H., Burrows, J. P., Buchwitz, M., Frerick, J., Noel, S., Rozanov, V. V., Chance, K. V., and Goede, A. P. H.: SCIAMACHY: Mission objectives and measurement modes, J. Atmos. Sci., 56, 127–150, 1999.

Bucsela, E. J., Perring, a. E., Cohen, R. C., Boersma, K. F., Celarier, E., Gleason, J. F., Wenig, M. O., Bertram, T. H., Wooldridge, P. J., Dirksen, R., and Veefkind, J. P.: Comparison of tropospheric NO$_2$ from in situ aircraft measurements with near-real-time and standard product data from OMI, J. Geophys. Res., 113, 1–14, doi:10.1029/2007JD008838, 2008.

Chai, T., Carmichael, G. R., Tang, Y., Sandu, A., Heckel, A., Richter, A., and Burrows, J. P.: Regional NO$_x$ emission inversion through a four-dimensional variational approach using SCIAMACHY tropospheric NO$_2$ column observations, Atmos. Environ., 43, 5046–5055, doi:10.1016/j.atmosenv.2009.06.052, 2009.

Eskes, H. J. and Boersma, K. F.: Averaging kernels for DOAS total-column satellite retrievals, Atmos. Chem. Phys., 3, 1285–1291, doi:10.5194/acp-3-1285-2003, 2003.

Eskes, H. J., Velthoven, P. F. J. V., Valks, P. J. M., and Kelder, H. M.: Assimilation of GOME total-ozone satellite observations in a three-dimensional tracer-transport model, Q. J. Roy. Meteorol. Soc., 129, 1663–1681, doi:10.1256/qj.02.14, 2003.

Evensen, G.: Sequential data assimilation with a nonlinear quasi-geostrophic model using Monte Carlo methods to forecast error statistics, J. Geophys. Res., 99, 10143–10162, doi:10.1029/94JC00572, 1994.

Graedel, T. E., Bates, T. S., Bouwman, A. F., Cunnold, D., Dignon, J., Fung, I., Jacob, D. J., Lamb, B. K., Logan, J. A., Marland, G., Middleton, P., Pacyna, J. M., Placet, M., and Veldt, C.: A compilation of inventories of emissions to the atmosphere, Global Biogeochem. Cy., 7, 1–26, 1993.

Houtekamer, P. L. and Mitchell, H. L.: Data Assimilation Using an Ensemble Kalman Filter Technique, Mon. Weather Rev., 126, 796–811, 1998.

Houtekamer, P. L. and Mitchell, H. L.: A Sequential Ensemble Kalman Filter for Atmospheric Data Assimilation, Mon. Weather Rev., 129, 123–137, 2001.

Hudman, R. C., Jacob, D. J., Turquety, S., Leibensperger, E. M., Murray, L. T., Wu, S., Gilliland, A. B., Avery, M., Bertram, T. H., Brune, W., Cohen, R. C., Dibb, J. E., Flocke, F. M., Fried, A., Holloway, J., Neuman, J. A., Orville, R., Perring, A., Ren, X., Sachse, G. W., Singh, H. B., Swanson, A., and Wooldridge, P. J.: Surface and lightning sources of nitrogen oxides over the United States: Magnitudes, chemical evolution, and outflow, J. Geophys. Res., 112, D12S05, doi:10.1029/2006JD007912, 2007.

Huijnen, V., Williams, J., van Weele, M., van Noije, T., Krol, M., Dentener, F., Segers, A., Houweling, S., Peters, W., de Laat, J., Boersma, F., Bergamaschi, P., van Velthoven, P., Le Sager, P., Eskes, H., Alkemade, F., Scheele, R., Nédélec, P., and Pätz, H.-W.: The global chemistry transport model TM5: description and evaluation of the tropospheric chemistry version 3.0, Geosci. Model Dev., 3, 445–473, doi:10.5194/gmd-3-445-2010, 2010.

Hunt, B. R., Kostelich, E. J., and Szunyogh, I.: Efficient data assimilation for spatiotemporal chaos: A local ensemble transform Kalman filter, Physica D, 230, 112–126, 2007.

IPCC: Climate Change 2007, The Physical Science Basis, Cambridge University Press, 2007.

Jaeglé, L., Steinberger, L., Martin, R. V., and Chance, K.: Global partitioning of NO$_x$ sources using satellite observations: Relative roles of fossil fuel combustion, biomass burning and soil emissions, Faraday Discuss., 130, 407–423, 2005.

Kalnay, E.: Ensemble Kalman Filter: Current status and potential, in: Data Assimilation: Making Sense of Observations, edited by: Lahoz, W., Khattatov, B., and Ménard, R., 69–92, Springer, 2010.

Kanamitsu, M., Ebisuzaki, W., Woollen, J., Yang, S.-K., Hnilo, J. J., Fiorino, M., and Potter, G. L.: NCEP-DOE AMIP-II Reanalysis (R-2), B. Am. Meteorol. Soc., 83, 1631–1643, doi:10.1175/BAMS-83-11-1631, 2002.

Kurokawa, J.-i., Yumimoto, K., Uno, I., and Ohara, T.: Adjoint inverse modeling of NO$_x$ emissions over eastern China using satellite observations of NO$_2$ vertical column densities, Atmos. Environ., 43, 1878–1887, doi:10.1016/j.atmosenv.2008.12.030, 2009.

Lamsal, L. N., Martin, R. V., van Donkelaar, A., Celarier, E. a., Bucsela, E. J., Boersma, K. F., Dirksen, R., Luo, C., and Wang, Y.: Indirect validation of tropospheric nitrogen dioxide retrieved from the OMI satellite instrument: Insight into the seasonal variation of nitrogen oxides at northern midlatitudes, J. Geophys. Res., 115, 1–15, doi:10.1029/2009JD013351, 2010.

Levelt, P. F., Hilsenrath, E., Leppelmeier, G. W., van Den Oord, G. H. J., Bhartia, P. K., Tamminen, J., De Haan, J. F., and Veefkind, P.: Science Objectives of the Ozone Monitoring Instrument, Geosci. Remote Sens., 44, 1199–1208, doi:10.1109/TGRS.2006.872336, 2006.

Lin, J.-T. and McElroy, M. B.: Impacts of boundary layer mixing on pollutant vertical profiles in the lower troposphere: Implications to satellite remote sensing, Atmos. Environ., 44, 1726–1739, doi:10.1016/j.atmosenv.2010.02.009, 2010.

Lin, J.-T., McElroy, M. B., and Boersma, K. F.: Constraint of anthropogenic NO$_x$ emissions in China from different sectors: a new methodology using multiple satellite retrievals, Atmos. Chem. Phys., 10, 63–78, doi:10.5194/acp-10-63-2010, 2010.

Martin, R., Jacob, D., Chance, K., Kurosu, T., Palmer, P., and Evans, M.: Global inventory of nitrogen oxide emissions constrained by space-based observations of NO$_2$ columns, J. Geophys. Res., 108, 1–12, doi:10.1029/2003JD003453, 2003.

Martin, R. V., Sauvage, B., Folkins, I., Sioris, C. E., Boone, C., Bernath, P., and Ziemke, J.: Space-based constraints on the production of nitric oxide by lightning, J. Geophys. Res., 112, 1–14, doi:10.1029/2006JD007831, 2007.

Ménard, R. and Chang, L.-P.: Assimilation of Stratospheric Chemical Tracer Observations Using a Kalman Filter. Part II: χ^2-Validated Results and Analysis of Variance and Correlation Dynamics, Mon. Weather Rev., 128, 2672–2686, 2000.

Miyoshi, T. and Yamane, S.: Local Ensemble Transform Kalman Filtering with an AGCM at a T159/L48 Resolution, Mon. Weather Rev., 135, 3841–3861, doi:10.1175/2007MWR1873.1, 2007.

Müller, J.-F. and Stavrakou, T.: Inversion of CO and NO$_x$ emissions using the adjoint of the IMAGES model, Atmos. Chem. Phys., 5, 1157–1186, doi:10.5194/acp-5-1157-2005, 2005.

Nagashima, T., Ohara, T., Sudo, K., and Akimoto, H.: The relative importance of various source regions on East Asian surface

ozone, Atmos. Chem. Phys., 10, 11305–11322, doi:10.5194/acp-10-11305-2010, 2010.

Napelenok, S. L., Pinder, R. W., Gilliland, A. B., and Martin, R. V.: A method for evaluating spatially-resolved NO$_x$ emissions using Kalman filter inversion, direct sensitivities, and space-based NO$_2$ observations, Atmos. Chem. Phys., 8, 5603–5614, doi:10.5194/acp-8-5603-2008, 2008.

Ohara, T., Akimoto, H., Kurokawa, J., Horii, N., Yamaji, K., Yan, X., and Hayasaka, T.: An Asian emission inventory of anthropogenic emission sources for the period 1980–2020, Atmos. Chem. Phys., 7, 4419–4444, doi:10.5194/acp-7-4419-2007, 2007.

Olivier, J. G. J., van Aardenne, J. A., Dentener, F., Pagliari, V., Ganzeveld, L. N., and Peters, J. A. H. W.: Recent trends in global greenhouse gas emissions: regional trends 1970-2000 and spatial distribution of key sources in 2000, Environ. Sci., 2, 81–99, 2005.

Ott, E., Hunt, B. R., Szunyogh, I., Zimin, A. V., Kostelich, E. J., Corazza, M., Kalnay, E., Patil, D. J., and Yorke, J. A.: A local ensemble Kalman filter for atmospheric data assimilation, Tellus A, 56, 415–428, doi:10.1111/j.1600-0870.2004.00076.x, 2004.

Price, C. and Rind, D.: A simple lightning parameterization for calculating global lightning distributions, J. Geophys. Res., 97, 9919–9933, 1992.

Randerson, J. T., van der Werf, G. R., Giglio, L., Collatz, G. J., and Kasibhatla, P. S.: Global Fire Emissions Database, Version 2 (GFEDv2.1). Data set, available at: http://daac.ornl.gov/, 2007.

Richter, A.: Satellite measurements of NO$_2$ from international shipping emissions, Geophys. Res. Lett., 31, 4–7, doi:10.1029/2004GL020822, 2004.

Sauvage, B., Gheusi, F., Thouret, V., Cammas, J.-P., Duron, J., Escobar, J., Mari, C., Mascart, P., and Pont, V.: Medium-range mid-tropospheric transport of ozone and precursors over Africa: two numerical case studies in dry and wet seasons, Atmos. Chem. Phys., 7, 5357–5370, doi:10.5194/acp-7-5357-2007, 2007.

Schaub, D., Brunner, D., Boersma, K. F., Keller, J., Folini, D., Buchmann, B., Berresheim, H., and Staehelin, J.: SCIAMACHY tropospheric NO$_2$ over Switzerland: estimates of NO$_x$ lifetimes and impact of the complex Alpine topography on the retrieval, Atmos. Chem. Phys., 7, 5971–5987, doi:10.5194/acp-7-5971-2007, 2007.

Singh, H. B., Brune, W. H., Crawford, J. H., Flocke, F., and Jacob, D. J.: Chemistry and transport of pollution over the Gulf of Mexico and the Pacific: spring 2006 INTEX-B campaign overview and first results, Atmos. Chem. Phys., 9, 2301–2318, doi:10.5194/acp-9-2301-2009, 2009.

Stavrakou, T., Müller, J.-F., Boersma, K. F., De Smedt, I., and van der A, R. J.: Assessing the distribution and growth rates of NO$_x$ emission sources by inverting a 10-year record of NO$_2$ satellite columns, Geophys. Res. Lett., 35, 1–5, doi:10.1029/2008GL033521, 2008.

Streets, D. G., Bond, T. C., Carmichael, G. R., Fernandes, S. D., Fu, Q., He, D., Klimont, Z., Nelson, S. M., Tsai, N. Y., Wang, M. Q., Woo, J. H., and Yarber, K. F.: An inventory of gaseous and primary aerosol emissions in Asia in the year 2000, J. Geophys. Res., 108, 8809, doi:10.1029/2002JD003093, 2003.

Sudo, K. and Akimoto, H.: Global source attribution of tropospheric ozone: Long-range transport from various source regions, J. Geophys. Res., 112, D12302,

doi:10.1029/2006JD007992, 2007.

Sudo, K., Takahashi, M., and Akimoto, H.: CHASER: A global chemical model of the troposphere 2. Model results and evaluation, J. Geophys. Res., 107, 4586, doi:10.1029/2001JD001114, 2002a.

Sudo, K., Takahashi, M., Kurokawa, J., and Akimoto, H.: CHASER: A global chemical model of the troposphere 1. Model description, J. Geophys. Res., 107, 4339, doi:10.1029/2001JD001113, 2002b.

Thornton, J. A., Wooldridge, P. J., Cohen, R. C., Williams, E. J., Hereid, D., Fehsenfeld, F. C., Stutz, J., and Alicke, B.: Comparisons of in situ and long path measurements of NO$_2$ in urban plumes, J. Geophys. Res., 108, 4496, doi:10.1029/2003JD003559, 2003.

U.S. EPA: Data from the National Emissions Inventory, Version 2.0. Data set, available at: http://www.epa.gov/ttn/chief/net/2005inventory.html, 2009.

van der A, R. J., Peters, D. H. M. U., Eskes, H., Boersma, K. F., van Roozendael, M., De Smedt, I., and Kelder, H. M.: Detection of the trend and seasonal variation in tropospheric NO$_2$ over China, J. Geophys. Res., 111, 1–10, doi:10.1029/2005JD006594, 2006.

van der A, R. J., Eskes, H. J., Boersma, K. F., van Noije, T. P. C., van Roozendael, M., De Smedt, I., Peters, D. H. M. U., and Meijer, E. W.: Trends, seasonal variability and dominant NO$_x$ source derived from a ten year record of NO$_2$ measured from space, J. Geophys. Res., 113, 1–12, doi:10.1029/2007JD009021, 2008.

van Noije, T. P. C., Eskes, H. J., Dentener, F. J., Stevenson, D. S., Ellingsen, K., Schultz, M. G., Wild, O., Amann, M., Atherton, C. S., Bergmann, D. J., Bey, I., Boersma, K. F., Butler, T., Cofala, J., Drevet, J., Fiore, A. M., Gauss, M., Hauglustaine, D. A., Horowitz, L. W., Isaksen, I. S. A., Krol, M. C., Lamarque, J.-F., Lawrence, M. G., Martin, R. V., Montanaro, V., Müller, J.-F., Pitari, G., Prather, M. J., Pyle, J. A., Richter, A., Rodriguez, J. M., Savage, N. H., Strahan, S. E., Sudo, K., Szopa, S., and van Roozendael, M.: Multi-model ensemble simulations of tropospheric NO$_2$ compared with GOME retrievals for the year 2000, Atmos. Chem. Phys., 6, 2943–2979, doi:10.5194/acp-6-2943-2006, 2006.

Velders, G., Granier, C., Portmann, R., Pfeilsticker, K., Wenig, M., Wagner, T., Platt, U., Richter, A., and Burrows, J.: Global tropospheric NO$_2$ column distributions- Comparing three-dimensional model calculations with GOME measurements, J. Geophys. Res., 106, 12643–12660, doi:10.1029/2000JD900762, 2001.

Volten, H., Brinksma, E. J., Berkhout, a. J. C., Hains, J., Bergwerff, J. B., van der Hoff, G. R., Apituley, A., Dirksen, R. J., Calabretta-Jongen, S., and Swart, D. P. J.: NO$_2$ lidar profile measurements for satellite interpretation and validation, J. Geophys. Res., 114, 1–18, doi:10.1029/2009JD012441, 2009.

Wang, Y., McElroy, M. B., Martin, R. V., Streets, D. G., Zhang, Q., and Fu, T.-M.: Seasonal variability of NO$_x$ emissions over east China constrained by satellite observations: Implications for combustion and microbial sources, J. Geophys. Res., 112, 1–19, doi:10.1029/2006JD007538, 2007.

Whitaker, J. and Hamill, T.: Ensemble data assimilation without perturbed observations, Mon. Weather Rev., 130, 1913–1924, 2002.

Yienger, J. and Levy, H.: Empirical model of global soil-biogenic NO$_x$ emissions, J. Geophys. Res., 100, 11447–11464, 1999.

Zhang, L., Jacob, D. J., Knipping, E. M., Kumar, N., Munger, J. W., Carouge, C. C., van Donkelaar, A., Wang, Y. X., and Chen, D.: Nitrogen deposition to the United States: distribution, sources, and processes, Atmos. Chem. Phys. Discuss., 12, 241–282, doi:10.5194/acpd-12-241-2012, 2012.

Zhao, C. and Wang, Y.: Assimilated inversion of NO$_x$ emissions over east Asia using OMI NO$_2$ column measurements, Geophys. Res. Lett., 36, 1–5, doi:10.1029/2008GL037123, 2009.

Zupanski, D. and Zupanski, M.: Model Error Estimation Employing an Ensemble Data Assimilation Approach, Mon. Weather Rev., 134, 1337–1354, doi:10.1175/MWR3125.1, 2006.